Magnesium and chromium isotope evidence for initial melting by radioactive decay of 26Al and late stage impact-melting of the ureilite parent body

van Kooten, Elishevah M. M. E.; Schiller, Martin; Bizzarro, Martin

Magnesium and chromium isotope evidence for initial melting by radioactive decay of ^{26}Al and late stage impact-melting of the ureilite parent body

Elishevah M.M.E. van Kooten[*], Martin Schiller, Martin Bizzarro

Centre for Star and Planet Formation and Natural History Museum of Denmark, University of Copenhagen, DK-1350 Copenhagen, Denmark

Abstract

Polymict ureilites are meteoritic breccias that provide insights into the differentiation history of the ureilite parent body. We have sampled a total of 24 clasts from the polymict ureilite Dar al Gani 319, representing a variety of lithologies such as mantle residues, cumulates and crustal fragments that are genetically related to monomict ureilites. In addition, we sampled four non-indigenous dark clasts and two chondrule-containing clasts from the same meteorite. We report on the petrology and the bulk mass-dependent and mass-independent magnesium and chromium isotope systematics of these clasts. The DaG 319 polymict ureilite consists predominantly of clasts related to Main Group ureilite residues (MG clasts) with varying Mg#s (0.74–0.91), as well as a significant fraction of olivine-orthopyroxene clasts related to Hughes Type ureilites (HT clasts) with consistently high Mg#s ($\sim$0.89). In addition, DaG 319 contains less abundant feldspathic clasts that are thought to represent melts derived from the ureilite mantle. A significant mass-dependent Mg-isotope fractionation totaling $\Delta\mu^{25}$Mg $= \sim$450 ppm was found between isotopically light feldspathic clasts (μ^{25}Mg $= -305 \pm 25$ to 15 ± 12 ppm), MG clasts (μ^{25}Mg $= -23 \pm 51$ ppm) and HT clasts (μ^{25}Mg $= 157 \pm 21$ ppm). We suggest that this isotopic offset is the result of equilibrium isotope fractionation during melting in the presence of an isotopically light magnesite component. We propose Mg-carbonates to be stable in the upper ureilite mantle, and pure carbon phases such as graphite to be stable at higher pressures. This is consistent with HT clasts lacking carbon-related phases, whereas MG clasts contain abundant carbon. The timing of differentiation events for the ureilitic clasts are constrained by high precision ^{53}Mn-^{53}Cr systematics and ^{26}Al-^{26}Mg model ages. We show that a dichotomy of ages exist between the differentiation of main group ureilite residues and HT cumulates rapidly after CAI formation and later remelting of cumulates with corresponding feldspathic melts, at 3.8 ± 1.3 Myr after CAI formation. Assuming an initial ^{26}Al/^{27}Al abundance $[(^{26}$Al/^{27}Al$)_0 = 1.33^{+0.21}_{-0.18} \times 10^{-5}]$ similar to the angrite parent body, the early melting event is best explained by heat production from ^{26}Al whereas the late event is more likely caused by a major impact. Variations in ^{54}Cr between MG clasts and HT clasts agree with a carbonaceous chondrite impactor onto the ureilite parent body. This impactor may be represented by abundant dark clasts found in polymict ureilites, which have μ^{26}Mg* and μ^{54}Cr signatures similar to CI chondrites. Similar volatile-rich dark clasts found in other meteorite breccias provide insights into the timing of volatile influx to the accretion region of the terrestrial planets.

1. INTRODUCTION

Achondrites are basaltic and plutonic fragments of differentiated asteroidal and planetary bodies. Having

* Corresponding author.

E-mail address: elishevah.vankooten@snm.ku.dk (E.M.M.E. van Kooten).

undergone most of their differentiation such as melting and crystallization in the first few million years of Solar System formation (Lugmair and Shukolyukov, 1998; Bizzarro et al., 2005; Amelin, 2008; Kleine et al., 2012; Schiller et al., 2010, 2011, 2015a), these meteorites provide insights into the earliest stages of the magmatic evolution of planets. Ureilites are the second most abundant group of achondrites and contain fragments of mostly mantle-derived materials, which can be divided into dominantly unbrecciated main group (or monomict) ureilites and rarer polymict (multiple clast types) ureilites. Most main group ureilites consist of olivine-pyroxene (dominantly pigeonite) mantle restites with varying magnesium numbers (Mg# = Mg/(Fe + Mg)), constant Mn/Mg ratios (Goodrich et al., 1987; Goodrich and Delaney, 2000) and high carbon abundances (∼3 wt.%). These characteristic features suggest that ureilites are the product of smelting reactions that reduce FeO-containing silicates to Fe-metal and Mg-rich silicates during partial melting in the presence of carbon (Goodrich et al., 1987, 2007; Warren and Kallemeyn, 1992; Walker and Grove, 1993; Singletary and Grove, 2003). Alternatively, the range of Mg#s can be explained by heterogeneous accretion of the ureilite parent body (UPB) (Warren and Kallemeyn, 1992; Warren and Huber, 2006; Warren, 2012). Monomict ureilites Mg#s correlate with oxygen isotope signatures of ureilites that fall on the Carbonaceous Chondrite Anhydrous Mineral (CCAM) line (Clayton and Mayeda, 1988, 1996), suggesting that these isotope signatures are of primitive origin (Sanders et al., 2017). However, rapid removal of partial melts formed during potential smelting can preserve initial heterogeneity of oxygen isotopes as well. Fast migration of melts is ensured by the smelting process, where the formation of CO and CO_2 gases contribute to explosive volcanism of partial melts, thereby potentially explaining the absence of these igneous rocks in our meteorite collection (Takeda, 1987; Warren and Kallemeyn, 1992; Scott et al., 1993). However, feldspathic clasts are present in polymict ureilites and are suggested to represent fragments of these SiO_2-rich melts (Ikeda and Prinz, 2001; Ikeda et al., 2003; Cohen et al., 2004; Bischoff et al., 2014). These plagioclase-rich clasts are small (<mm-sized) fragments with variable textures and compositions (Cohen et al., 2004), ranging from mafic (olivine-augite and anorthite-rich) to felsic mineralogies (albite-rich) indicating different degrees of fractional crystallization and cooling histories. Polymict ureilites also contain clasts of monomict ureilites (type I ureilitic clasts; Ikeda et al., 2000), olivine-orthopyroxene-augite clasts similar to a group of unusual ureilites typified by Hughes 009 (type II ureilitic clasts; Ikeda et al., 2000; Ikeda and Prinz, 2001; Goodrich et al., 2001) and olivine-augite clasts that are thought to represent para-cumulates (Goodrich et al., 2004).

The paradoxical blend of high degree partial melting (∼25–30%) required to produce the composition of the olivine-pigeonite restites (Scott et al., 1993; Goodrich, 1999; Goodrich et al., 2007), together with noble gas signatures (Göbel et al., 1978), siderophile trace element patterns in metal (Rankenburg et al., 2008), anomalous nitrogen (Grady and Pillinger, 1988) and oxygen isotope signatures

that resemble that of primitive chondrites (Clayton and Mayeda, 1988, 1996), complicates the development of a ureilite differentiation model that satisfies all constraints. For example, the timeline and stages of magmatic differentiation based on the groupings of feldspathic clasts (one-stage or multi-stage) and the effect of the disruptive event that formed the polymict ureilites remain unresolved. Most of these issues have been addressed by melting models that have used major elements, trace elements and rare earth element (REE) patterns to constrain the physical conditions of differentiation and the chemical nature of the UPB and its precursor material (Singletary and Grove, 2003; Goodrich et al., 2007; Barrat et al., 2016b). In addition, ^{26}Al-^{26}Mg, ^{53}Mn-^{53}Cr and ^{182}Hf-^{182}W short-lived isotope, as well as U-Pb and ^{176}Lu-^{176}Hf long-lived isotope systematics have been used to constrain the formation history of feldspathic clasts and monomict ureilites (Kita et al., 2003, 2007; Goodrich et al., 2010; Qin et al., 2010b; Yamakawa et al., 2010; Bischoff et al., 2014; Amelin et al., 2015; Budde et al., 2015; Bast et al., 2016). However, the lack of an established genetic relationship between these feldspathic clasts and other ureilite components limits their use to develop a unified model for the magmatic evolution of the UPB. More precise isochron data may reveal previously unseen relationships between different lithologies.

The focus of this work lies therefore in defining genetic relationships between various igneous reservoirs of the UPB and constraining its differentiation history by using the ^{26}Al-^{26}Mg and ^{53}Mn-^{53}Cr short-lived radioisotope systems along with mass-dependent magnesium and chromium isotope compositions. The combination of chronology of magmatic processes, mass-dependent isotope fractionation patterns and ^{54}Cr nucleosynthetic anomalies can be utilized to outline the physical processes that resulted in the differentiation of the UPB. The various ureilitic components (e.g., feldspathic, type I and type II ureilite clasts) were sampled from the polymict ureilite Dar al Gani 319, which is well known for the diversity of its ureilitic clasts (Ikeda et al., 2000, 2003; Ikeda and Prinz, 2001; Cohen et al., 2004). In addition, we have sampled a variety of chondritic clasts present in this meteorite to identify the nature of potential precursor materials to the UPB. We describe relationships between various ureilitic clasts and provide a timeline for a two-stage differentiation history of the UPB. Furthermore, we provide constraints on the chemical and physical mechanisms involved in these differentiation events.

2. SAMPLES

Samples from this study were taken from the polymict ureilite DaG 319 and general descriptions of these clast types are given in overview Table 1, whereas detailed descriptions, images and compositional data of individual samples and their phases can be found in the Electronix Annex. DaG 319 is a micro-breccia and multiple clasts have been studied extensively for their mineralogy, petrology, trace element and oxygen isotope composition (Ikeda et al., 2000, 2003; Ikeda and Prinz, 2001; Cohen et al., 2004; Goodrich et al., 2004; Kita et al., 2004, 2006).

Table 1

Overview of clast types studied in this work. Detailed descriptions, images and compositional data for individual clasts and their phases are described in the Electronic Annex. Samples for which no data is available are depicted by 'nm', not measured. MG clasts = Main Group clasts, HT clasts = Hughes Type clasts.

Classification	Description	Mg#	size	vol.%
MG clasts (type I ureilite clasts)	Seperate olivine and pyroxene fragments and ol-px clasts with abundant carbon veins	0.74–0.91	~1 mm	>90
HT clasts (type II ureilite clasts, Hughes cluster)	Agglomerates of euhedral olivine with interstitial orthopyroxene (Al_2O_3 = 1.1–1.3 wt%), no intraclast carbon	~0.89	>5 mm	>10
Feldspathic clasts	Albitic, labrodoritic and olivine-augite lithologies	0.5–1.0 (Px), 0.7–0.9 (Ol)	<1 mm	<2
Dark clasts	Fine-grained phyllosilicate matrix with abundant Fe sulfides, magnetite and dolomitic carbonates	nm	<5 mm	<2
Chondrule-containing clasts	Porphyritic-olivine chondrules in a fine-grained highly altered sulfide-rich matrix	nm	~1 mm	<0.5

Although monomict ureilite clasts dominate in DaG 319, this meteorite also contains a variety of feldspathic igneous clasts that may be indigenous to the UPB (<2 vol.%) as well as chondritic clasts (<2 vol.%).

For the purpose of Mg- and Cr-isotope analyses, we sampled the following clasts:

(1) We sampled nine *type I ureilitic clasts* as defined by Ikeda et al. (2000) that are identical to monomict ureilites (hereafter MG clasts, main group clasts). These clasts were mainly present as separate entities of mm-sized olivine and pyroxene with a wide range of Mg#s (Fo ~74–92). We sampled four olivine and four pyroxene clasts in addition to one clast containing both minerals.

(2) We sampled five clasts classified as *type II ureilitic clasts* or *Hughes Type ureilites* (hereafter HT clasts, Hughes Type clasts; Ikeda et al., 2000; Goodrich et al., 2001). These clasts are cm-sized objects containing olivine and low-Ca pyroxene (Wo < 5) with a narrow range of high Mg#s (Fo ~90).

(3) Ten *feldspathic clasts* were sampled, which were generally smaller (<1 mm) than MG clasts and include albitic, olivine-augite and labradoritic lithologies (Cohen et al., 2004).

(4) Lastly, we sampled six chondritic clasts. Four of these are *primitive carbonaceous clasts* or 'dark clasts', which make up the bulk of the chondritic clasts in DaG 319 and were previously considered as potential precursor material to the UPB (Ikeda et al., 2003). Dark clasts are fragments of carbonaceous chondrites consisting of hydrothermally altered chondritic matrix. They have so far been classified as CI (Ivuna-type) and CM (Mighei-type) like clasts based on the composition of their phyllosilicates (serpentine-smectite solid solution) and the presence of sulfides and magnetite. Oxygen isotope compositions of dark clasts typically follow the CCAM line, but also plot above the terrestrial fractionation line (Clayton and Mayeda, 1988). In addition to the dark clasts, two chondritic clasts that contain chondrules were sampled.

3. ANALYTICAL METHODS

3.1. Mineral chemistry

Initial investigations of the DaG 319 meteorite were conducted on polished thick sections using the Phillips XL40 scanning electron microscope located at the Geological Survey of Denmark and Greenland. Back scattered electron images (BSE) were taken of all samples selected for Mg- and Cr-isotope analyses, along with semi-quantitative elemental maps by energy dispersive spectroscopy (EDS). Quantitative compositional information of individual minerals was retrieved by electron microprobe with the JEOL JXA-8200 Superprobe at the University of Copenhagen. The microprobe operated at 15 keV accelerating voltage, with a 15 nA beam current and a fully focused

4 µm beam using five wavelength dispersive spectrometers. Sample analyses were carried out along standard measurements of in house silicates and oxides, described in Sandrin et al. (2009).

3.2. Magnesium and chromium isotope analyses

DaG 319 clasts were sampled from the thick sections with the computer-assisted NewWave micro-drill, using tungsten carbide drill bits at the Centre for Star and Planet formation (Copenhagen). Powders from the drilled samples were transferred with double distilled MQ water to clean Savillex beakers. Olivine and pyroxene-rich samples (MG and HT clasts) were typically between 0.5 and 1.0 mg in size, whereas feldspathic clasts samples were smaller, yielding <100 µg of sample material. This resulted in 100–400 µg Mg and 2–10 µg Cr for MG and HT clasts and 2–10 µg Mg and 60–500 ng of Cr for feldspathic clasts. To avoid contaminations from surrounding material, which can potentially have very contrasting Mg- and Cr-isotope signatures, care was taken not to drill close to the clast boundaries. After drilling, the individual drill spots were examined visually under a microscope for possible contamination. Any samples where contamination was suspected were discarded. Samples were digested first on a hotplate at 150 °C in a mixture of concentrated HNO_3/HF acid for 2 days and subsequently for 1 day in Parr bombs at 210 °C. Afterwards, sample solutions were dried down and treated with aqua regia for one more day. Olivine and pyroxene MG clasts were not completely dissolved at this point, due to remaining carbon residues. These samples were further treated for 3 additional days in concentrated HNO_3/HF, using Parr-bombs at 210 °C. After this treatment, all Cr and Mg was in solution (including potential ilmenite and spinel grains that have previously been observed in ureilitic materials) and ready for elemental purification by ion exchange chromatography. A 5% aliquot was taken from the sample solutions before commencing with the purification process and used to determinate the $^{27}Al/^{24}Mg$ and $^{55}Mn/^{52}Cr$ ratios on the ThermoFisher X-series quadrupole Ionization Coupled Plasma Mass Spectrometer (ICPMS) at the Centre for Star and Planet Formation (Copenhagen), which are accurate to 2%. Purification of Mg and Cr was done by methods described in Bizzarro et al. (2011) and Van Kooten et al. (2016).

The isotopic composition of the purified Mg was determined by the standard-sample bracketing technique using the Neptune Plus Multi Collector (MC)-ICPMS at the Natural History Museum of Denmark based on protocols described in Bizzarro et al. (2011) and Van Kooten et al. (2016). Samples were typically analyzed with a signal intensity of 20–45 V on mass ^{24}Mg (all collectors are connected to amplifiers with 10^{11} Ω feedback resistors) for smaller feldspathic samples and 80–100 V (^{24}Mg was measured on a detector connected to a 10^{10} Ω feedback resistor, whereas ^{25}Mg and ^{26}Mg were measured on detectors connected to 10^{11} Ω feedback resistors) for larger samples. Apart for two feldspathic clasts that did not contain sufficient amounts of Mg, all samples we systematically analyzed ten times (Table 2). Mg-isotope data are reported in the

µ-notation as deviations from the DTS-2b standard [$\mu^{25}Mg_{DSM-3} = -122 \pm 17$ ppm (2SD, Bizzarro et al., 2011)] according to the following formula:

$$\mu^x Mg = \left[\frac{(^xMg/^{24}Mg)_{sample}}{(^xMg/^{24}Mg)_{DTS\text{-}2b}} - 1 \right] \times 10^6 \qquad (1)$$

where x represents mass 25 or 26. The mass-independent component of ^{26}Mg ($\mu^{26}Mg^*$) is reported in the same fashion, but represents deviations from the internally normalized $^{26}Mg/^{24}Mg$ of the sample from the reference standard, normalized to $^{25}Mg/^{24}Mg = 0.126896$ (Bizzarro et al., 2011) using the exponential mass fractionation law. All Mg data reduction was conducted off-line using the Iolite data reduction package which runs within Igor Pro (Paton et al., 2011) and changes in mass bias with time were interpolated using a smoothed cubic spline. For each analysis, the mean and standard error of the measured ratios were calculated using a 2SD threshold to reject outliers. Individual analyses of a sample were combined to produce an average weighted by the propagated uncertainties of individual analyses and reported final uncertainties are the 2SE of the mean. The external reproducibility of the technique utilized here to acquire our Mg isotope data has been estimated by Bizzarro et al. (2011) to be 20 and 2.5 ppm for the ^{25}Mg and $^{26}Mg^*$, respectively. This estimate is based on the repeated analysis of various terrestrial rock standards as well as extraterrestrial samples. In the current study, we have verified that our external reproducibility is in line with earlier estimates, through repeated analysis of individual column-processed rock digestion aliquots of various USGS terrestrial rock standards acquired over a one-year period that coincide with the time the data reported in this paper were acquired. In detail, we analyzed four aliquots of the BHVO-2 standard and seven aliquots of the DTS-2b standard. Note that nine out of the 11 standard analyses were reported in Olsen et al. (2016) and Van Kooten et al. (2016). Based on these data, we derive an external reproducibility of 22 and 2.5 for the ^{25}Mg and $^{26}Mg^*$, respectively, which is in line with the estimate reported by Bizzarro et al. (2011) using the same technique.

The Cr-isotope composition of all samples was measured by thermal ionization mass spectrometry (Triton TIMS) at the Centre for Star and Planet Formation. We used the small chemistry column purification techniques described by Schiller et al. (2014), which we adapted to include a last purification step to remove sodium and to minimize organics and elemental impurities introduced during the separation. This step utilizes an Eichrom AG50 X8 200–400 mesh cation resin and sample pretreatments to ensure full recovery of Cr after removing residual unwanted impurities (i.e., organics, Na, Fe, Ti, Al) that can cause matrix effects or interference on the Cr signal. First, the samples are pretreated in 50 µl 1 M HNO_3 + 10 µl concentrated H_2O_2 for >5 days at room temperature to promote the speciation of Cr^{3+} (Larsen et al., 2016a). Subsequent dilution to a 0.5 M HNO_3 loading solution and elution of 1.3 ml of 0.5 M HNO_3 on a 100 µl cation resin, resulted in the removal of Na, K and organics. Adding an additional three column volumes of 1 M HF removed any remaining

Table 2

μ^{25}Mg isotope data for ureilitic clasts and terrestrial standards with corresponding μ^{26}Mg* values corrected for kinetic (kin) and equilibrium (eq) fractionation law. μ^{25}Mg isotope data are presented relative to DTS-2b and DSM-3 terrestrial rock standards. The DSM-3 standard is isotopically heavier than Earth's mantle and deviates from DTS-2b by μ^{25}Mg $= 122 \pm 17$ ppm (Bizzaro et al., 2011). Ab = albitic, OA = olivine-augite and lab = labradoritic. Internal errors are presented as 2SE.

	^{27}Al/^{24}Mg	μ^{25}Mg$_{DTS}$	μ^{25}Mg$_{DSM3}$	μ^{26}Mg*$_{kin}$	μ^{26}Mg*$_{eq}$	n
Terrestrial standards						
DTS-2b (1)		7.0 ± 5.0	129.0 ± 17.7	0.5 ± 2.0		10
DTS-2b (2)		0.3 ± 0.6	122.3 ± 17.0	0.7 ± 1.5		10
Dark clasts						
LC2b	0.098	-22 ± 5	100 ± 18	5.8 ± 1.6		10
LC3	0.099	16 ± 5	138 ± 18	4.3 ± 2.0		10
LC4	0.111	-15 ± 19	107 ± 26	5.9 ± 2.4		10
LC6	0.099	18 ± 2	140 ± 17	8.6 ± 1.2		10
Average		-0.75 ± 41		6.2 ± 3.6		
Unidentified chondritic clasts						
TR7	0.114	-55 ± 20	67 ± 26	-1.8 ± 2.8	-3.8 ± 3.0	10
BSa4	0.114	-141 ± 15	-19 ± 23	0.4 ± 3.0	-5.2 ± 3.3	9
RT3 (remolten)	0.326	-193 ± 18	-71 ± 25	-2.5 ± 2.7	-7.1 ± 3.2	10
Main Group clasts						
WB3	0.019	-22 ± 10	100 ± 20	-7.9 ± 1.9	-9.0 ± 2.2	10
WB4	0.020	-30 ± 14	92 ± 22	-9.5 ± 1.6	-8.5 ± 1.7	10
WB5	0.001	11 ± 7	133 ± 19	-10.6 ± 1.0	-10.4 ± 1.0	10
BSa5	0.005	-50 ± 14	72 ± 22	-14.2 ± 2.3	-14.5 ± 1.8	10
Average	0.011	-23 ± 51		-10.6 ± 5.3	-10.6 ± 5.4	
Hughes type clasts						
WB1	0.003	166 ± 5	288 ± 18	3.4 ± 1.8	10.1 ± 2.4	10
DUO1-1	0.005	135 ± 22	257 ± 28	-0.9 ± 1.0	5.0 ± 1.8	10
DUO2-1	0.005	170 ± 22	292 ± 28	-1.7 ± 1.7	6.3 ± 3.0	10
RT2	0.006	157 ± 10	279 ± 20	5.6 ± 2.2	10.9 ± 2.8	10
TR4	0.005	157 ± 11	279 ± 20	5.0 ± 2.5	7.9 ± 3.6	10
Average	0.005	157 ± 27		2.3 ± 6.8	8.0 ± 5.0	
Feldspathic clasts						
DUO2-3 (Ab)	5.324	-183 ± 33	-61 ± 37	24.9 ± 3.5	17.1 ± 4.4	9
BSa2 (Ab)	1.410	-72 ± 28	50 ± 33	12.5 ± 4.1	10.1 ± 5.3	10
BSb1 (Ab)	0.663	-69 ± 19	53 ± 26	2.3 ± 3.8	-1.9 ± 5.1	10
RT1a (Ab)	1.584	-181 ± 10	-59 ± 20	-2.3 ± 3.9	-7.6 ± 3.7	5
RT1b (Ab)	0.699	-305 ± 25	-183 ± 30	-2.1 ± 5.8	-15.4 ± 4.0	3
WB2 (Lab)	0.077	-75 ± 16	47 ± 23	3.4 ± 2.5	1.4 ± 2.7	10
DUO1-2 (OA)	0.106	15 ± 12	137 ± 21	8.5 ± 1.3	9.4 ± 1.7	10
BSa3 (OA)	0.146	-189 ± 11	-67 ± 20	-7.5 ± 2.5	-13.4 ± 3.2	10
TR3 (OA)	0.109	-34 ± 15	88 ± 23	-8.9 ± 2.4	-8.3 ± 3.7	10

trace of Fe, Al and Ti. Cr was then collected by elution with 6 M HCl. Cr yields are typically >95% and washes of samples with lower yields were subjected to an additional cycle of the last cation purification step and recombined. Chromium isotope analyses were conducted using a hybrid method of total evaporation and standard-sample bracketing fully described in Van Kooten et al. (2016). Samples were typically measured 16 times distributed over multiple sessions. Smaller samples were measured using fewer filaments according to their sample size (1 filament = 15 ng). The SRM-3112a standard was measured concurrently over all sessions. Cr-isotope data is presented in the ε-notation relative to this standard:

$$\varepsilon^x Cr = \left[\frac{(^xCr/^{52}Cr)_{sample}}{(^xCr/^{52}Cr)_{SRM-3112a}} - 1 \right] \times 10^4 \qquad (2)$$

where x represents mass 53 and 54 and the ^{54}Cr/^{52}Cr values reflect the internally normalized values, normalized to ^{52}Cr/^{50}Cr $= 19.2832$ (Trinquier et al., 2008a) using the exponential mass fractionation law. Individual analyses of a sample were combined to produce an average weighted by the propagated uncertainties of individual analyses and reported final uncertainties are the 2SE of the mean using a 2SD outlier rejection scheme. From terrestrial rock standards (e.g., DTS-2b, BHVO-2) processed in this work and Van Kooten et al. (2016) that were measured over the same period as our samples, we estimate an external reproducibility of 6 ppm (2SD) and 12 ppm on mass-bias corrected ε^{53}Cr and ε^{54}Cr values, respectively.

Additional mass-dependent Cr-isotope measurements by MC-ICPMS were carried out on six MG and four HT clasts. Of these, one MG clast and all HT clasts were also

analyzed by TIMS. Mass-dependent Cr-isotope analyses were carried out by standard-sample bracketing following procedures described in Schiller et al. (2014) at the Centre for Star and Planet Formation (Copenhagen) with the Neptune Plus MC-ICPMS. Interferences from argon oxides and nitrides on the ^{52}Cr, ^{53}Cr and ^{54}Cr signal were minimized by using a trifluoro-methane (CHF_3) supplementary gas and running in a 'cold plasma' mode with an RF power of 700 W. At high resolution this reduced the $^{40}Ar^{16}O$ and $^{40}Ar^{14}N$ signals to below 0.5 V and 0.2 V, respectively. Analyses were carried out on the low-mass side of the Cr peak, typically at mass 51.908. This peak position was confirmed before each standard analysis by peak centering on the ^{50}Cr peak, which is the isotope least affected by gas based interferences. All samples were analyzed as ~1 ppm solutions and a 25 μl/min uptake rate, which resulted in a total Cr beam of ~20 V. Each individual sample run comprised 834 s (16.77 s × 50 blocks), consuming ~400 ng. Each sample was run five times, whereas the DTS-2b standard was run 20 times. All data was reduced using the Iolite software package in Igor Pro. Changes in mass bias with time were interpolated using a smoothed cubic spline and data are presented as the weighted mean and 2SE error. Repeated analyses of the DTS-2b rock standard using this setup resulted in an external reproducibility of 12 ppm (2SD) and 28 ppm on internally normalized ε^{53}Cr and ε^{54}Cr values, respectively. Mass-dependent Cr-isotopes are presented in the δ-notation:

$$\delta^x Cr = \left[\frac{(^xCr/^{52}Cr)_{sample}}{(^xCr/^{52}Cr)_{SRM-3112a}} - 1 \right] \times 10^3 \qquad (3)$$

where x represent mass 50, 53 and 54. During measurements, interferences of ^{50}Ti, ^{50}V and ^{54}Fe on ^{50}Cr and ^{54}Cr were monitored by measuring ^{49}Ti, ^{51}V and ^{56}Fe signals. The interference of ^{50}V on ^{50}Cr was typically <1 ppm of signal strength, whereas those of ^{50}Ti on ^{50}Cr and ^{54}Fe on ^{54}Cr were one or two orders of magnitude larger, respectively. Corrections of <10^4 ppm on ^{54}Fe yielded accurate and reproducible ε^{54}Cr values (Schiller et al., 2014). This resulted in an external reproducibility of 28 ppm on δ^{50}Cr.

4. RESULTS

4.1. Compositions of DaG 319 clasts

4.1.1. Main Group (MG) and Hughes Type (HT) clasts

Thick sections of the DaG 319 meteorite are dominated (~90 vol.%) by mm-sized olivine and pyroxene grains similar to monomict ureilites (Fig. 1a). Pyroxenes are present in lower abundances and are generally smaller (<1 mm). These MG clasts are typically mono-mineralic crystals interspersed in a fine-grained groundmass consisting of smaller ureilitic clasts, sulfides, FeNi-metal, dark clasts and carbon-rich matter. Some MG clasts also occur as agglomerates of olivine and pyroxene. Olivine clasts typically have relatively thin rims (<100 μm) that are Mg-poor with respect to their cores and most clasts contain veins of carbon-rich

matter (see Electronic Annex). Main Group clasts have variable magnesium numbers (Mg# = Mg/(Fe + Mg)) ranging from 0.74–0.91, but have constant Mn/Mg ratios (Fig. 2; Electronic Annex, Tables S2 and S3). Main Group pyroxenes and olivines fall on different slopes in Fe/Mg versus Fe/Mn space, as shown previously by Goodrich and Delaney (2000). In contrast, the HT clasts in these sections (<10 vol.%) are generally more Mg-rich and have a very narrow range of Mg#s (~0.89; Electronic Annex, Table S1). Hughes Type clasts are named for their resemblance to unusual ureilites similar to Hughes 009, since the Mn/Mg ratios of HT olivines are generally offset from the linear correlation determined for MG clasts and correspond to Hughes Type compositions (Fig. 2; Downes et al., 2008). However, HT clasts are distinct from Hughes Type ureilites in that their pyroxene Mn/Mg ratios fall on the trend for MG pyroxenes and are, thus, offset from the field characterizing pyroxenes from Hughes Type ureilites. In addition, Hughes Type ureilites contain 7–52 vol.% augite and 23–47 vol.% olivine (Goodrich et al., 2001), whereas HT clasts from DaG 319 contain relatively low-Ca pyroxenes and olivine contents of >40 vol.% (Electronic Annex, Table S1 and Fig. S4). Hughes Type clasts are typically mm- to cm-sized and contain fairly euhedral, submm olivine (Fig. 1b) surrounding mostly anhedral pyroxenes that are enriched in Al compared to MG clasts pyroxenes (typically 1.2–1.3 wt % Al_2O_3; Electronic Annex, Tables S2 and S3). Olivine and pyroxene grains show triple junctions with 120° angles and have no preferred orientation.

4.1.2. Feldspathic clasts

A detailed classification and description of the feldspathic (plagioclase-bearing) clasts in DaG 319 has been previously reported by Ikeda and Prinz (2001) and Ikeda et al. (2003). Their classification is based on texture and further divides feldspathic clasts into porphyritic, pilotaxitic, glassy and gabbroic types. Furthermore, Cohen et al. (2004) defined multiple populations of feldspathic clasts (albitic, labradoritic, olivine-augite) based on their mineralogy and texture. Most of the feldspathic clasts analyzed here are albitic (n = 8), one sample is labradoritic and three samples have an olivine-augite composition (Fig. 1, see also Electronic Annex). Albitic clasts have varying porphyritic textures: (1) Three of the clasts contain a groundmass of albitic feldspar (An < 5) with embedded needle-shaped enstatite crystals (Fig. 1c), (2) four clasts are dominated by albite with typically minor anhedral pigeonite-augite phenocrysts (Fig. 1d) and (3) one clast contains relatively large (>100 μm) euhedral phenocrysts of enstatite and albite in a pilotaxitic matrix of pyroxene with plagioclase needles (Fig. 1e). The labradoritic clast is dominated by enstatite phenocrysts in a labradoritic groundmass with An ~70 (Fig. 1f). Two out of three olivine-augite feldspathic clasts have a porphyritic texture with forsterite and augite phenocrysts embedded in an albitic groundmass (Fig. 1g), whereas one clast is dominated by augite and contains minor forsterite and albite (Fig. 1h). Similar to MG and HT clasts, olivine-augite and labradoritic clasts are characterized by pyroxene with high Mg#s between 0.8 and 1.0 (Electronic Annex, Table S4), whereas albitic clasts
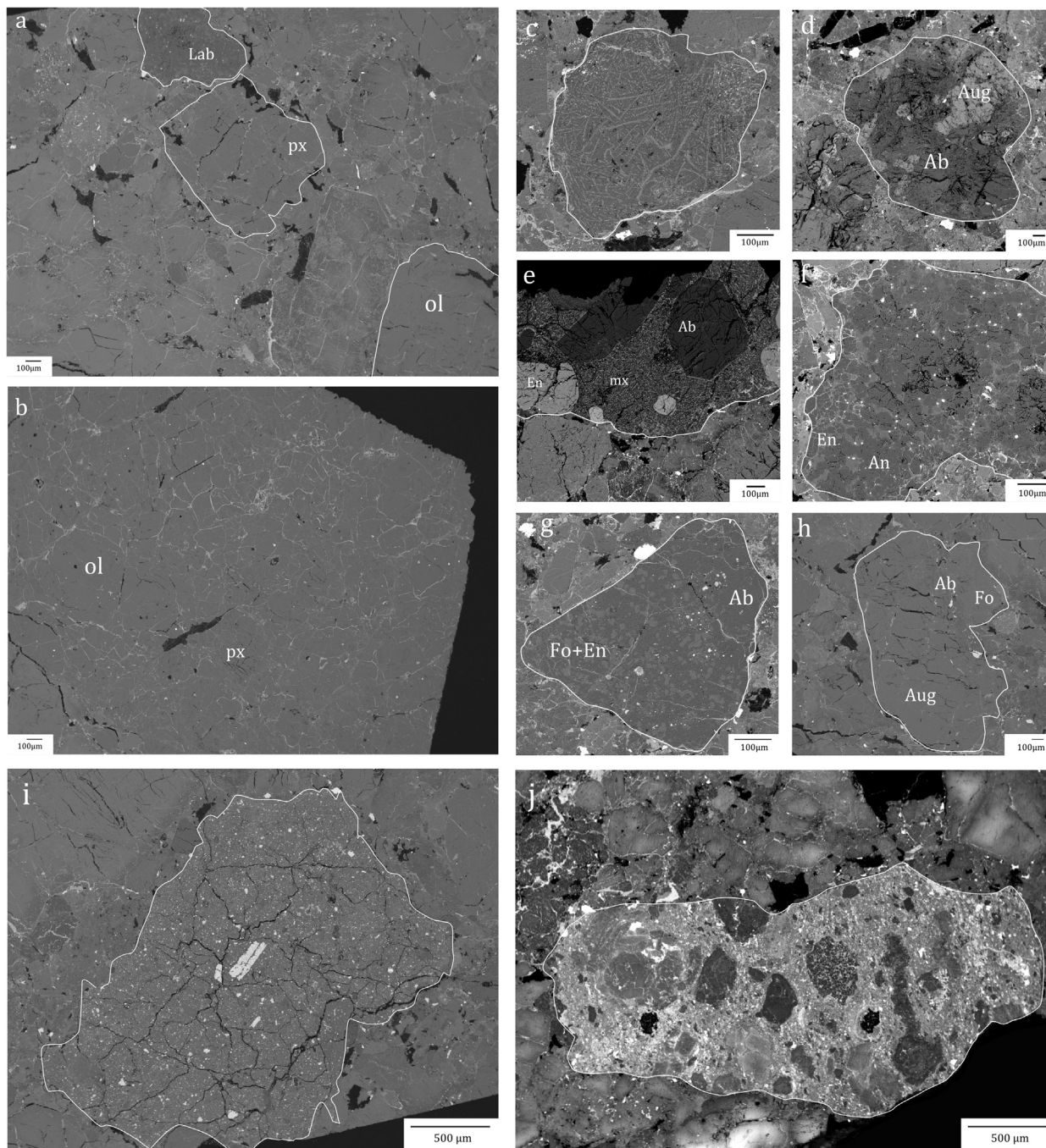
Fig. 1. Compilation of back scattered electron images from various clast types in the DaG 319 polymict ureilite, with (a) typical distribution of clast types, with mostly main group/monomict (MG) clasts of olivine (ol) and more rare pyroxene (px), where the in white lineated clasts (WB2, 3, 4) are sampled for Mg- and Cr-isotope analyses; (b) WB1: olivine-orthopyroxene (HT) clast; (c) RT1a (like RT1b, BSb1): albitic clast with enstatite needles; (d) BSa2: albitic clast with augite phenocrysts; (e) DUO2-3: Albitic clast with albite (Ab) and enstatite (En) phenocrysts; (f) WB2: labradoritic clast with En and anorthite (An); (g) RT3 (like BSa3, TR3): olivine-augite feldspathic clast in albitic groundmass; (h) DUO1-2: olivine-augite clast with minor albite; (i) LC6: Dark clast with sulfides, magnetite and carbonates in a phyllosilicate matrix and (j) TR7: chondrule-containing clast.

have pyroxenes with intermediate Mg#s (0.5–0.7). All pyroxenes in feldspathic clasts have variable Mn/Mg ratios and fall on a trend determined for fractional crystallization from the main ureilite body (Fig. 2). Of these clasts, two clasts show shock-related textures: clasts BSa3 and TR3 contain melt pockets between albite grains with augite compositions. Clast RT3 contains a granoblastic texture of porphyritic augite and olivine, which is indicative of recrystallization during thermal overprinting (Electronic Annex, Fig. S8).
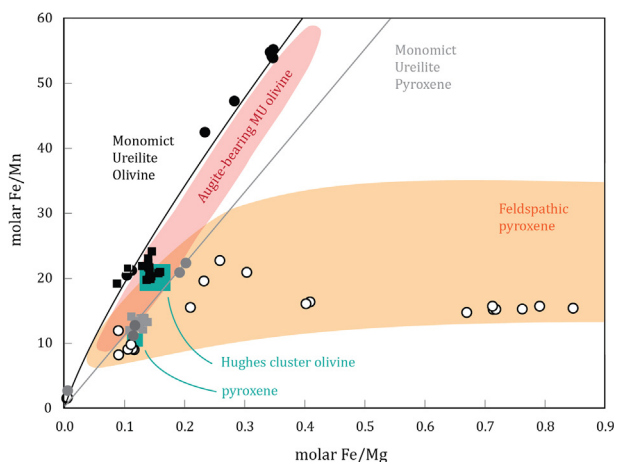
Fig. 2. Molar Fe/Mg vs. Fe/Mn in pyroxenes and olivines from main group clasts (black spheres: olivine, gray spheres: pyroxenes) falling on the redox trends established by Goodrich et al. (1987) and Goodrich and Delaney (2000). Olivines from HT clasts (Ol: black squares) are offset from the main group olivine line and correlate with Hughes cluster ureilites (green square; Downes et al., 2008). HT clasts enstatite compositions (En: gray squares) fall on the main group pyroxene trend, whereas Hughes cluster pyroxenes are off this line. Albitic, olivine-augite and labradorite feldspathic lithologies from this study (white spheres) all fall on a normal igneous fractionation trend (Cohen et al., 2004). No distinction can be made between these clasts on this fractionation trend.

4.1.3. Other clasts

All dark clasts in DaG 319 analyzed here are fayalite-free (Ikeda et al., 2003; Fig. 1i). The clasts contain Mg-rich phyllosilicates such as serpentine and smectite, are rich in iron sulfides and contain to a lesser extent magnetite and dolomitic carbonates, with rare ilmenite. One other type of chondritic clast was recognized in the sections, which contains porphyritic-olivine chondrules in a fine-grained highly altered matrix that is very rich in sulfides (Fig. 1j).

4.2. Magnesium isotopes

4.2.1. Mass-dependent Mg-isotope compositions

Magnesium isotope compositions for all measured DaG 319 samples are presented in Table 2 and Fig. 3. The different clast types (MG, HT and feldspathic clasts) are defined by variable amounts of mass-dependent Mg-isotope fractionation. Main Group clasts have slightly lighter isotope compositions than Earth's mantle, with $\mu^{25}Mg$ values between -50 ± 14 ppm and -11 ± 7 ppm. Hughes Type clasts are significantly heavier than Earth's mantle and exhibit a narrow range of $\mu^{25}Mg$ values with an average of 157 ± 27 ppm (2SD, $n = 5$). The feldspathic clasts have variable but generally light Mg-isotope compositions with $\mu^{25}Mg$ values ranging from -305 ± 25 ppm up to $+15 \pm 12$ ppm. The four analyzed dark clasts have similar magnesium isotope compositions ($\mu^{25}Mg = -1 \pm 41$ ppm, 2SD), whereas the two chondrule-containing clasts TR7 and BSa4 have $\mu^{25}Mg$ compositions of -55 ± 20 ppm and -141 ± 15 ppm, respectively.

4.2.2. ^{26}Al-^{26}Mg systematics

The mass-independent $\mu^{26}Mg^*$ composition (mass-bias corrected using the kinetic law) of the various clasts indicate variable excesses of $\mu^{26}Mg^*$ compared to the Solar System initial of -15.9 ± 2.5 ppm as defined by the canonical isochron consisting of calcium-aluminum-inclusions and amoeboid olivine aggregates (CAI and AOA; Larsen et al., 2011). Main Group clasts have low $^{27}Al/^{24}Mg$ ratios of 0.011 ± 0.020 and an average $\mu^{26}Mg^*$ value of -10.6 ± 5.3 ppm (2SD) (Fig. 4), which is in agreement with previous measurements of bulk monomict ureilites ($\mu^{26}Mg^* = -8.3 \pm 0.5$ ppm, Larsen et al., 2011; $\mu^{26}Mg^* = -7.1 \pm 6.3$, Baker et al., 2012). These clasts have significantly lower $\mu^{26}Mg^*$ values than HT clasts with similar $^{27}Al/^{24}Mg$ ratios of 0.005 ± 0.002 and an average $\mu^{26}Mg^*$ value of 2.3 ± 6.3 ppm (2SD). Given the difference of 200 ppm in the Mg mass-dependent isotope composition of MG clasts and HT clasts, we calculate the effects of kinetic and equilibrium isotope fractionation on the $\mu^{26}Mg^*$ values of these clasts (Table 2). We show that correcting the Mg-isotope data by equilibrium ($\mu^{26}Mg^*_{eq}$) instead of kinetic ($\mu^{26}Mg^*_{kin}$) fractionation law has little effect on the $\mu^{26}Mg^*$ values for MG clasts ($\mu^{26}Mg^*_{eq} = -10.6 \pm 5.4$ ppm), but increases the $^{26}Mg^*$ for HT clasts ($\mu^{26}Mg^*_{eq} = 8.0 \pm 5.0$ ppm) and significantly lowers the spread in data as indicated by a reduction in MSWD values from 15 for $\mu^{26}Mg^*_{kin}$ to 4.7 for $\mu^{26}Mg^*_{eq}$. This suggests that mass-dependent Mg-isotope fractionation exhibited by HT clasts is best explained by equilibrium rather than kinetic law, since we expect no variation in $\mu^{26}Mg^*$ values for clasts that appear to be co-genetic based on very constant Mg#s and Mn/Mg ratios and a narrow range of $\mu^{25}Mg$ values.

Labradoritic and olivine-augite feldspathic clasts ($n = 4$) have $^{27}Al/^{24}Mg$ ratios between 0.077 and 0.146 and have varying $\mu^{26}Mg^*_{kin}$ values ranging between -8.9 ± 2.4 ppm and 8.5 ± 1.3 ppm (Fig. 4). Albitic clasts ($n = 6$) have higher $^{27}Al/^{24}Mg$ ratios ranging from 0.6 to 5.3 with $\mu^{26}Mg^*$ excesses between -8.1 ± 2.2 ppm and 24.9 ± 3.5 ppm. Unlike HT clasts, we cannot point to a superior isotope fractionation law for feldspathic clasts (e.g., equilibrium or kinetic mass-bias corrected $\mu^{26}Mg^*$), since the spread in $\mu^{26}Mg^*$ values is at least in part related to variations in $^{27}Al/^{24}Mg$.

The four analyzed dark clasts have $\mu^{26}Mg^*$ values ranging between 4.3 ± 2.0 ppm and 8.6 ± 1.2 ppm, with an average of $\mu^{26}Mg^* = 6.2 \pm 3.6$ ppm (2SD). These values are comparable with CI-type carbonaceous chondrites (Larsen et al., 2011). The chondrule-containing clasts have $\mu^{26}Mg^*$ values of -3.8 ± 3.0 ppm and -5.2 ± 3.3 ppm for TR7 and BSa4, respectively. Their Mg-isotope compositions suggest a link to ordinary chondrites (Larsen et al., 2011).

4.3. Chromium isotopes

4.3.1. Mass-dependent Cr-isotope compositions

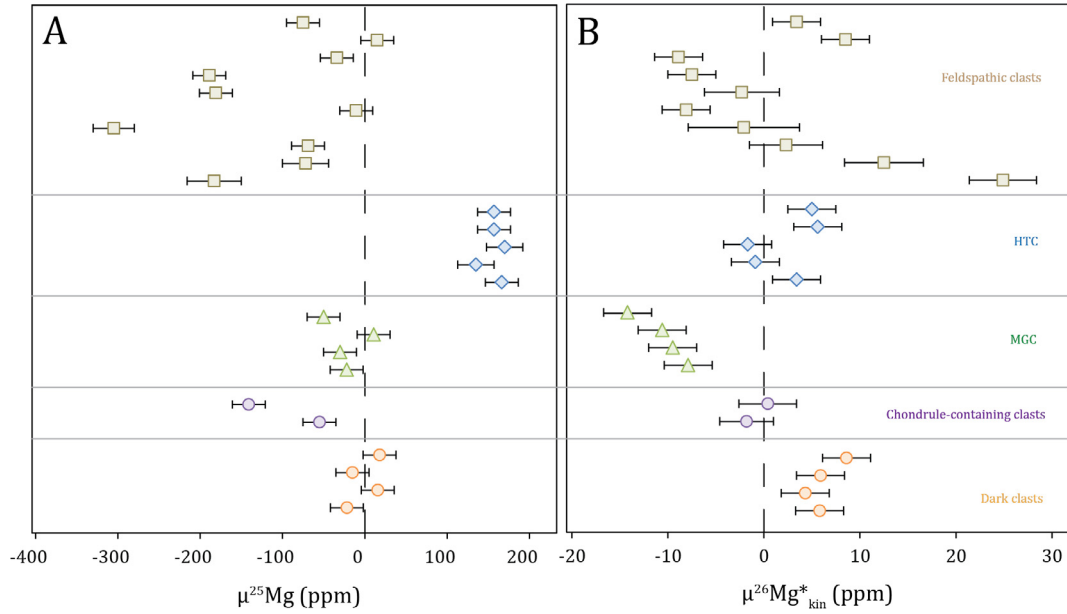The $^{50}Cr/^{52}Cr$ ratios of MG and HT clasts were obtained by MC-ICPMS and are presented in Table 3

Fig. 3. Magnesium isotope data for various clasts from the polymict ureilite DaG 319. Left panel: mass-dependent Mg-isotope compositions presented as $\mu^{25}Mg$ values. Right panel: Mass-bias corrected $\mu^{26}Mg^*$ compositions using kinetic law. Dashed line represents Earth's mantle. Errors are presented as 2SE internal or external values (2.5 ppm on $\mu^{26}Mg^*$ and 20 ppm on $\mu^{25}Mg$), whichever one is larger.

and Fig. 5. The accuracy and reproducibility of this method has been tested by repeat analyses of the dunite DTS-2b rock standard, yielding a $\delta^{50}Cr$ value of 0.314 ± 0.006. This is in good agreement with the value of 0.320 ± 0.096 (2SD) for DTS-2b obtained by Schiller et al. (2014). Analyses of MG and HT clasts show that there is a resolvable Cr-isotope difference of $\sim$190 ppm between the two group averages (Fig. 5), where $\delta^{50}Cr$ is 0.140 ± 0.090 (2SD) for five MG clasts and 0.331 ± 0.080 (2SD) for HT clasts. Thus, in contrast to the $\mu^{25}Mg$ values, the $\delta^{50}Cr$ values indicate a lighter stable isotope composition for HT clasts relative to MG clasts.

4.3.2. $\varepsilon^{54}Cr$ values

Cr-isotope data obtained by TIMS are presented in Table 4 and Fig. 6. We analyzed four MG clasts that have $\varepsilon^{54}Cr$ values ranging between -1.10 ± 0.12 and -0.74 ± 0.07 (Fig. 6b). This data range is confirmed by MC-ICPMS data from BSa5 and five additional MG clasts with $\varepsilon^{54}Cr$ values between -1.28 ± 0.29 and -0.74 ± 0.05 (Table 3). The average $\varepsilon^{54}Cr$ value of -0.94 ± 0.11 (2SE) for MG clasts is in agreement with literature data for monomict ureilites [$\varepsilon^{54}Cr = -1.08 \pm 0.25$ (2SE), Larsen et al., 2011; $\varepsilon^{54}Cr = -0.92 \pm 0.02$ (2SE), Yamakawa et al., 2010], but is ^{54}Cr-depleted relative to multiple ureilitic fragments from the polymict ureilite Almahata Sitta [$\varepsilon^{54}Cr = -0.77 \pm 0.03$ (2SE), Qin et al., 2010b]. The HT clasts have overall more positive $\varepsilon^{54}Cr$ values than the MG clasts and, with an average of -0.79 ± 0.10 (2SE), are thus closer in composition to Almahata Sitta. The $\varepsilon^{54}Cr$ data for HT individual clasts as well as their average [$\varepsilon^{54}Cr = -0.79 \pm 0.14$ (2SE)] obtained by TIMS are reproduced by MC-ICPMS, highlighting the accuracy between
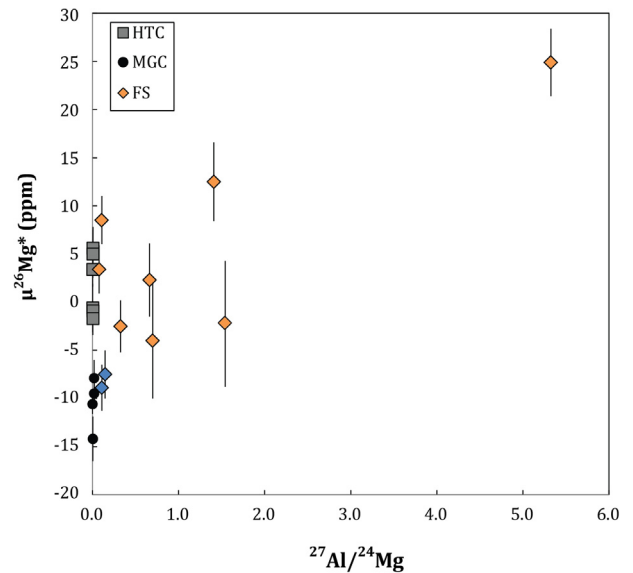

Fig. 4. A $\mu^{26}Mg^*$ versus $^{27}Al/^{24}Mg$ diagram with data for HT clasts, MG clasts and feldspathic (FS) clasts. Shock altered clasts BSa3 and TR3 are represented by blue diamonds.

both approaches and suggesting an offset in $\varepsilon^{54}Cr$ between MG and HT clasts of up to 15 ppm. In Fig. 7a, we plot $\varepsilon^{54}Cr$ values of MG and HT analyses against their $\delta^{50}Cr$ values, in which we show that no significant correlation exists. If anything, $\delta^{50}Cr$ seems to increase with $\varepsilon^{54}Cr$, an effect that is opposite to what is expected from equilibrium isotope fractionation-related $\varepsilon^{54}Cr$ excesses (Fig. 7b). However, recalculating HT clast $\varepsilon^{54}Cr$ values with an equilibrium law (in a similar approach to Mg-isotopes) reduces

the 2SD value to 0.22 as opposed to kinetic law yielding a 2SD of 0.35. Similar to the mass-dependent Mg-isotope data, this reduction in scatter suggests that the HT-related reservoir is affected by equilibrium isotope fractionation of Cr.

The analyzed feldspathic clasts show relatively large variations in $\varepsilon^{54}Cr$ (Table 4). Their range spans from -1.18 ± 0.11, similar to MG clasts, up to 1.16 ± 0.5 for clast TR3. The bulk of feldspathic clasts have $\varepsilon^{54}Cr$ values between -1.18 ± 0.11 and -0.54 ± 0.15. We note that the anomalously high $\varepsilon^{54}Cr$ value of clast TR3 may be related to its shock-melting history (see Electronic Annex). The small size of the feldpathic clasts (<500 ng Cr) did not allow for repeat analyses by MC-ICPMS. The dark clasts from DaG 319 range from $\varepsilon^{54}Cr = 1.30 \pm 0.12$ to 1.86 ± 0.11, averaging around the CI carbonaceous chondrite value of 1.56 ± 0.13 (2SD, Shukolyukov and Lugmair, 2006; Trinquier et al., 2007; Qin et al., 2010a; Van Kooten et al., 2016). Combined with their $\mu^{26}Mg^{*}$ composition, this suggests that the dark clasts are closely related to CI chondrites. The chondrule-containing clasts have $\varepsilon^{54}Cr$ values of -0.09 ± 0.15 and 0.40 ± 0.40 (Table 4) corresponding to ordinary and enstatite chondrites with average bulk values of -0.34 ± 0.14 and $+0.08 \pm 0.10$, respectively (Trinquier et al., 2007; Qin et al., 2010b).

4.3.3. ^{53}Mn-^{53}Cr systematics

In Fig. 6a, we present $\varepsilon^{53}Cr$ data from MG and HT clasts together with literature data from whole rock monomict ureilites (Yamakawa et al., 2010) and Almahata Sitta fragments (Qin et al., 2010b). Main Group clasts have an average $\varepsilon^{53}Cr$ composition of 0.13 ± 0.14 (2SD), which is similar to monomict ureilites. This average value is confirmed by MC-ICPMS analyses on BSa5 and five additional MG clasts [Table 3; $\varepsilon^{53}Cr = 0.12 \pm 0.21$ (2SD)]. Corresponding $^{55}Mn/^{52}Cr$ ratios of MG clasts range between 0.5 and 0.8, in agreement with data from Yamakawa et al. (2010) for monomict ureilites. In contrast, HT clasts
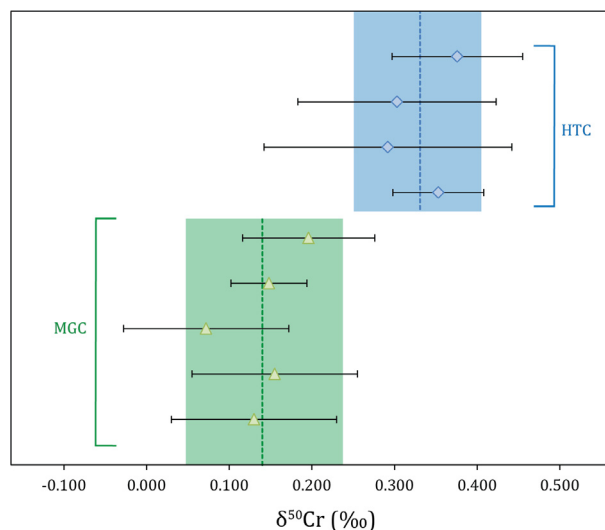

Fig. 5. Chromium mass-dependent isotope data for MG and HT clasts. Individual data represent means with 2SE internal or external errors, whichever one is larger, whereas green and blue boxes represent averaged values with 2SD error for MG and HT clasts, respectively.

have higher $^{55}Mn/^{52}Cr$ ratios of ~1.2 and $\varepsilon^{53}Cr$ values that average 0.43 ± 0.06 (2SD). Almahata Sitta fragments consist of lithologies that are similar to both MG clasts and HT clasts (Zolensky et al., 2010) and have $\varepsilon^{53}Cr$ values and corresponding $^{55}Mn/^{52}Cr$ ratios that fall between monomict ureilites reported by Yamakawa et al. (2010) and HT clasts in this work (Fig. 8). The $\varepsilon^{53}Cr$ data for individual feldspathic clasts varies from 0.07 ± 0.06 to 1.31 ± 0.27 (2SE). In Fig. 8, we present $\varepsilon^{53}Cr$ versus $^{55}Mn/^{52}Cr$ data of MG clasts and HT clasts, as well as data from Yamakawa et al. (2010) and Qin et al. (2010b). Our results from sampled main group olivine and pyroxene cores (MG clasts) plot on a slope equivalent to $(^{53}Mn/^{55}Mn)_0 = (6.8$

Table 3
Mass-dependent Cr-isotope data and mass-bias corrected $\varepsilon^{53}Cr$ and $\varepsilon^{54}Cr$ data for ureilite clasts measured by MC-ICPMS. Internal errors are presented as 2SE.

	$^{55}Mn/^{52}Cr$	$\varepsilon^{54}Cr$	$\varepsilon^{53}Cr$	$\delta^{50}Cr$
Terrestrial standards				
DTS-2b (3)		0.04 ± 0.06	0.03 ± 0.03	0.314 ± 0.006
Main group clasts				
BSa5 (olpx)	0.5570	-0.74 ± 0.06	0.09 ± 0.07	0.369 ± 0.027
BSbpx (px)	0.4978	-1.28 ± 0.29	-0.05 ± 0.10	0.130 ± 0.015
DUO1px (px)	0.7200	-0.82 ± 0.29	0.14 ± 0.10	0.155 ± 0.027
Bsapx (px)	0.7603	-0.94 ± 0.18	0.19 ± 0.10	0.072 ± 0.024
DUO1ol (ol)	0.5210	-0.91 ± 0.09	0.22 ± 0.05	0.148 ± 0.005
WBOl7 (ol)	0.7310	-0.79 ± 0.14	0.11 ± 0.08	0.196 ± 0.017
Average	0.6311	-0.95 ± 0.39	0.12 ± 0.21	0.140 ± 0.090
Hughes type clasts				
DUO1-1 (olpx)	1.1578	-0.83 ± 0.16	0.35 ± 0.55	0.353 ± 0.032
DUO2-1 (olpx)	1.1732		0.30 ± 0.15	0.292 ± 0.016
RT2 (olpx)	1.1116	-0.66 ± 0.23	0.54 ± 0.12	0.303 ± 0.029
TR4 (olpx)	1.1818	-0.90 ± 0.15	0.42 ± 0.08	0.376 ± 0.010
Average	1.1561	-0.79 ± 0.25	0.40 ± 0.21	0.331 ± 0.080

Table 4

$\varepsilon^{53}Cr$ and $\varepsilon^{54}Cr$ values of ureilitic clasts measured by TIMS. N is the amount of analyses done for each sample. Internal errors for individual clasts are given in 2SE. Average values are presented with a 2SD error.

	$^{55}Mn/^{52}Cr$	$\varepsilon^{54}Cr$	$\varepsilon^{53}Cr$	n
Terrestrial standards				
DTS-2b (2)		-0.03 ± 0.13	0.06 ± 0.05	28
Dark clasts				
LC2b	0.7877	1.44 ± 0.18	-0.03 ± 0.07	16
LC3	0.6979	1.30 ± 0.12	-0.07 ± 0.04	14
LC4	0.6922	1.58 ± 0.18	-0.05 ± 0.05	10
LC6	0.5790	1.86 ± 0.11	0.15 ± 0.05	14
Average		1.55 ± 0.48	0.00 ± 0.20	
Chondritic clasts				
TR7	0.6103	-0.09 ± 0.15	0.22 ± 0.08	10
BSa4	0.7135	0.40 ± 0.40	0.37 ± 0.05	5
Main group clasts				
WB3 (px)	0.5069	-1.10 ± 0.12	0.04 ± 0.03	14
WB4 (ol)	0.8000	-0.90 ± 0.18	0.19 ± 0.11	15
WB5 (ol)	0.7044	-0.98 ± 0.13	0.12 ± 0.05	16
BSa5	0.5570	-0.74 ± 0.07	0.18 ± 0.04	16
Average		-0.93 ± 0.30	0.13 ± 0.14	
Hughes type clasts				
WB1	1.1797	-0.86 ± 0.08	0.4 ± 0.05	14
DUO1-1	1.1578	-0.89 ± 0.11	0.46 ± 0.06	16
DUO2-1	1.1732	-0.83 ± 0.09	0.42 ± 0.06	16
RT2	1.1116	-0.61 ± 0.09	0.47 ± 0.03	11
TR4	1.1818	-0.75 ± 0.11	0.41 ± 0.06	5
Average		-0.79 ± 0.22	0.43 ± 0.06	
Feldspathic clasts				
DUO2-3 (Ab)	3.9447	-0.72 ± 0.08	1.29 ± 0.09	16
BSa2 (Ab)	1.0117	-0.62 ± 0.08	0.40 ± 0.06	16
BSb1 (Ab)	0.6364	-1.18 ± 0.11	0.07 ± 0.06	11
RT1b (Ab)	0.5967	-0.54 ± 0.15	0.44 ± 0.10	8
BSa3 (OA)	1.5000	-0.56 ± 0.25	1.31 ± 0.27	8
DUO1-2 (OA)	0.3894	-0.91 ± 0.15	0.21 ± 0.05	8
RT3 (OA)	0.6809	0.02 ± 0.14	0.24 ± 0.04	6
BSa3 (OA)	1.5000	-0.56 ± 0.25	1.31 ± 0.27	8
TR3 (Ab)	1.4400	1.16 ± 0.50	1.18 ± 0.11	3
Average		-0.76 ± 1.52	0.70 ± 1.08	

$\pm 2.0) \times 10^{-6}$, which is steeper than found from bulk ureilite data by Yamakawa et al. (2010) and Qin et al. (2010b) (Table 5). Feldspathic clasts (excluding BSa3 and TR3) fall on a slope $[(^{53}Mn/^{55}Mn)_0 = (3.7 \pm 1.5) \times 10^{-6}]$ that is within error of the slope from Yamakawa et al. (2010), Qin et al. (2010b) and Goodrich et al. (2010) (Table 5). HT clasts fall on the intersect of the feldpathic and MG clast slope (Fig. 8).

Dark clasts, despite their similar $\varepsilon^{54}Cr$ signatures, have slightly lower $^{55}Mn/^{52}Cr$ ratios ($^{55}Mn/^{52}Cr = 0.58$–0.79) relative to CI chondrites ($^{55}Mn/^{52}Cr = 0.85$, Trinquier et al., 2008b) as well as lower $\varepsilon^{53}Cr$ values [$\varepsilon^{53}Cr = 0.00 \pm 0.20$ (2SD) for dark clasts, $\varepsilon^{53}Cr = 0.32 \pm 0.18$ (2SD) for CI chondrites; Shukolyukov and Lugmair, 2006; Trinquier et al., 2007; Qin et al., 2010a; Van Kooten et al., 2016]. Lower $^{55}Mn/^{52}Cr$ abundances correlated with reduced bulk $\varepsilon^{53}Cr$ values for these dark clasts suggests a

differences in precursor materials, rather than variations related to parent body processes.

5. DISCUSSION

5.1. Origin of the Mg mass-dependent isotope fractionation

Our $\mu^{25}Mg$ data indicate a significant amount of mass-dependent Mg-isotope fractionation between various ureilitic clasts that translates into a range of ~ 450 ppm. Feldspathic clasts display a wide range of isotopically light Mg compositions ($\mu^{25}Mg = -305 \pm 25$ ppm to $+15 \pm 12$ ppm), whereas HT clasts consistently record heavy Mg-isotope signatures ($\mu^{25}Mg = 157 \pm 27$ ppm). Main Group clasts are intermediate between these groups with $\mu^{25}Mg$ values between -50 ± 14 ppm and -11 ± 7 ppm. We discuss below potential mechanisms that can account for the observed mass-dependent Mg-isotope fractionation.

5.1.1. Initial Mg-isotope heterogeneity

An important mechanism to discuss is the possibility that all variation is caused by initial heterogeneity of mass-dependent Mg-isotopes during accretion of polymict ureilites or of the initial UPB. This would either suggest that the clasts are not genetically related to each other or that, similarly to oxygen isotopes, this initial heterogeneity was preserved during parent body processes (Clayton and Mayeda, 1988; Clayton and Mayeda, 1996). However, the total amount of variation in $\mu^{25}Mg$ values found for Solar System planetary reservoirs is approximately 100 ppm (Larsen et al., 2016b), suggesting that the relatively large variation found in ureilitic clasts cannot be accounted for by heterogeneity alone.

5.1.2. Equilibrium isotope fractionation

Partial melting and/or fractional crystallization can cause equilibrium isotope fractionation for which the partition coefficient is dependent on the relative difference in coordination numbers of the element of interest in both minerals and melts (Schauble, 2011). In the case of magnesium isotopes, tetrahedral sites in minerals are preferentially occupied by the heavier isotopes, whereas light isotopes prefer the octahedral sites. For example, spinel with Mg occupying tetrahedral sites has a higher $\mu^{25}Mg$ value than co-genetic silicates like olivine or pyroxene with Mg occupying octahedral sites. Silicate melts are thought to contain a mixture of tetrahedral, pentrahedral and octahedral sites that is dependent on their composition (Wilding et al., 2004; Henderson et al., 2006) and should, thus, be isotopically heavier than co-genetic silicates (Schauble, 2011). Although for terrestrial reservoirs (e.g., mid-ocean ridge basalts, ocean island basalts and Earth's mantle), the amount of Mg equilibrium fractionation during differentiation appears to be small (Schiller et al., 2010; Teng et al., 2007, 2010; Huang et al., 2011), mass-dependent Mg-isotope fractionation has been observed during magmatic differentiation on asteroids (Schiller et al., 2017). Thus, if feldspathic clasts are partial melts with relatively high Mg coordination numbers, these clasts should be isotopically heavier than their residues. In contrast to this
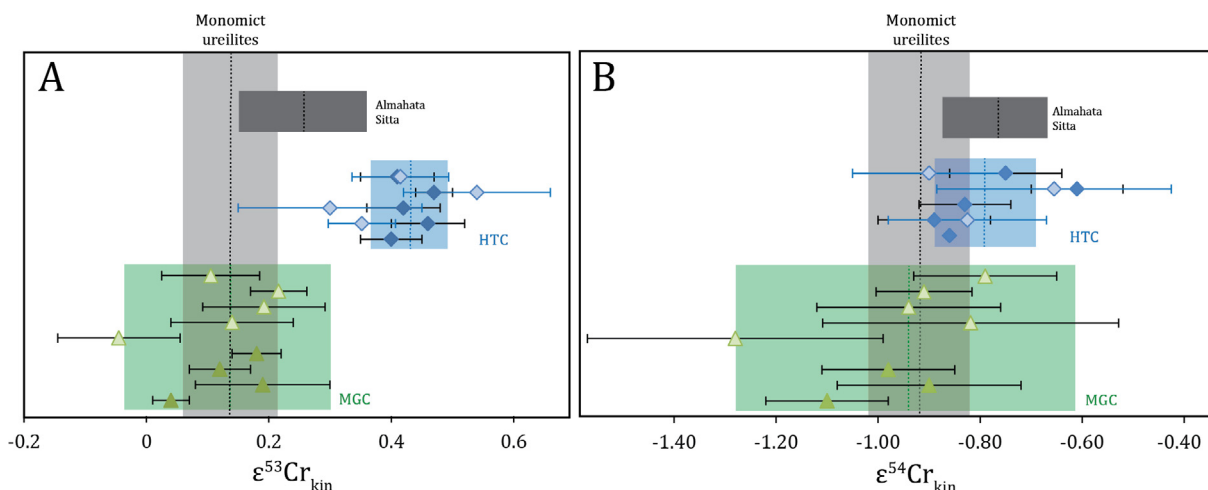
Fig. 6. Chromium isotope mass-bias corrected data for MG and HT clasts from TIMS (dark green and blue) and MC-ICPMS (light green and blue) analyses. HT clasts Cr-isotope data presented on the same row are analyzed from the same aliquots by TIMS and MC-ICPMS. Green and blue bars represent averaged values with a 2SD error. Data for whole rock monomict ureilites and Almahata Sitta fragments are from Yamakawa et al. (2010) and Qin et al. (2010b), respectively. Errors are presented as 2SE internal or external values, whichever one is larger.

prediction, the clasts are lighter than main ureilite body clasts by up to 250 ppm and lighter than HT clasts by up to 450 ppm.

A possible solution to this apparent contradiction is the presence of a magnesite component in the partial melt with a low Mg coordination number, which should be isotopically light relative to co-genetic silicates (Schauble, 2011; Yang et al., 2012). As a result, the isotope effect is opposite to that of 'normal' equilibrium isotope fractionation such that the magnesite-containing melt will be depleted in the heavy Mg-isotopes relative to the residue. The stability of magnesite in the ureilite mantle is dependent on pressure, temperature and oxygen fugacity. At lower pressures and temperatures, oxidized carbon becomes stable over pure carbon phases such as graphite over a larger range of oxygen fugacities (Goodrich et al., 2007; Stagno and Frost, 2010; Stagno et al., 2011). We show in Fig. 9 the stability of graphite in a pressure versus fO_2 diagram, where with increasing temperature, graphite is stable over $CO + CO_2$ at lower pressures. The modeled peak temperature for equilibrated ureilite residues (1276 °C, Goodrich et al., 2007) results in the stability of CO and CO_2 over carbon in the upper ~5 km of the ureilite mantle. In Earth's mantle, the $C–CO + CO_2$ equilibrium line defines the transition between graphite and magnesite, or between diamond and magnesite in the lower mantle (Stagno and Frost, 2010; Stagno et al., 2011). Hence, we show in Fig. 9 that the upper ureilite mantle may be characterized by the presence of oxidized carbon as a stable mantle phase, whereas in the lower mantle carbon is reduced to graphite. Pure carbon phases are so far observed in ureilite mantle residues defined as 'type I ureilite clasts' (Ikeda et al., 2000; Kita et al., 2004) or MG clasts in this work, whereas carbon veins are absent in crystals from 'type II ureilite clasts' or HT clasts in this work. Hence, MG clasts with their range of Mg#s, may represent smelting-related residues derived

from varying depths in the stability regime of pure carbon, whereas HT clasts may be derived from shallower mantle regions compatible with magnesite. We emphasize that the smelting process is not necessary to invoke separate stability regimes for carbon and magnesite.

To discuss the potential presence of magnesite in HT clasts it is relevant to first consider the magmatic origin of HT clasts, which represent either cumulates or residues from the ureilite mantle. They can be linked through Fe/Mg versus Mn/Mg ratios of their olivines and pyroxenes to the unusual Hughes Type ureilites (Fig. 2), which are suggested to represent cumulates (Downes et al., 2008). However, unlike Hughes Type ureilites, HT clasts have a higher abundance of olivine (>40 vol.%) and do not contain high-Ca pyroxenes such as augite. On Earth, such peridotite compositions (e.g., harzburgites) are rarely associated with cumulate origins. Furthermore, HT clasts do not show a characteristic crystal alignment expected for cumulates (Electronic Annex, Fig. S4). Collectively, the petrological features of HT clasts indicate that they are residues, although their mixed characteristics suggest that they may have experienced multiple differentiation events and may have primarily formed as cumulates. We interpret that the low carbon abundances (Goodrich et al., 2001; Ikeda and Prinz, 2001; Kita et al., 2004) and high $\mu^{25}Mg$ values of HT clasts relative to MG clasts suggest that HT clasts represent cumulates from which a isotopically light magnesite melt component was extracted. These low $\mu^{25}Mg$ values are recorded by the feldspathic clasts. It is possible to roughly estimate the amount of magnesite necessary to produce the isotopic differences observed between HT clasts and feldspathic clasts, since similar effects are observed on Earth. Terrestrial basalts from the North China craton are found to be on average 150 ppm lighter for $\mu^{25}Mg$ than their source mantle peridotites (Yang et al., 2012). This is attributed to a 20% dolomitic melt derived from carbonated
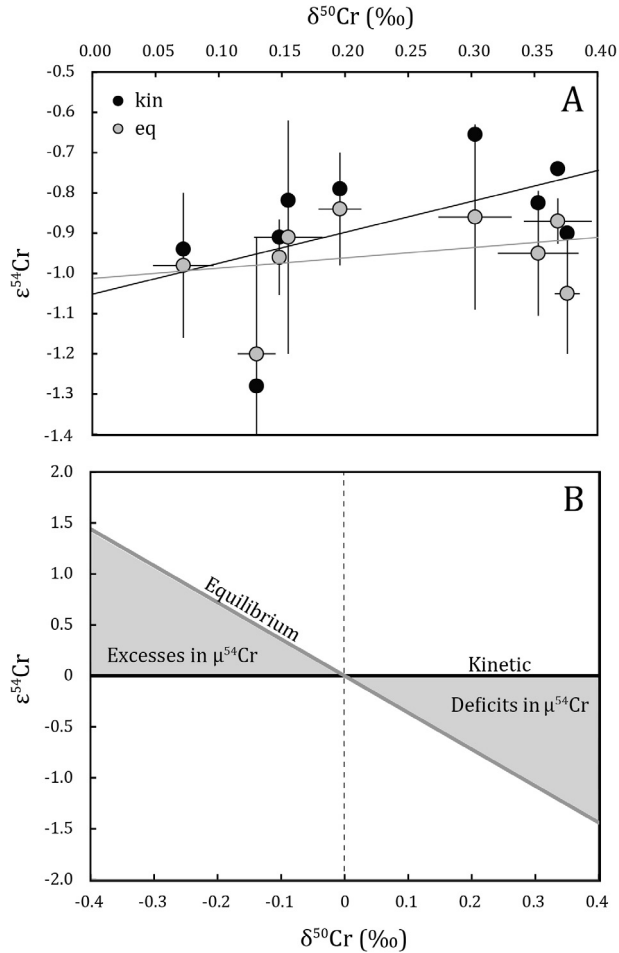
Fig. 7. Plots showing variation of $\varepsilon^{54}Cr$ with the amount of mass-dependent isotope fractionation depicted by $\delta^{50}Cr$ for MG and HT clasts in (a) and theoretical fractionation in (b). (a) The ureilite clasts show a total amount of mass-dependent isotope fractionation of ∼350 ppm, while the average $\Delta\delta^{50}Cr$ is ∼200 ppm between MG and HT clasts. Data is corrected for kinetic fractionation law ($\beta = 0.505$, black circles) and for equilibrium fractionation law ($\beta = 0.509$, gray circles). Error bars are only shown for gray circles for clarity. This plot shows that with equilibrium fractionation, there is no resolvable variation in $\varepsilon^{54}Cr$ (2SD = 0.22), whereas with kinetic law there seems to be a positive correlation between $\varepsilon^{54}Cr$ and $\delta^{50}Cr$ (2SD = 0.35). (b) Apparent excesses and deficits for $\varepsilon^{54}Cr$ created by mass-dependent Cr isotope fractionation for hypothetical samples, which illustrates that 100 ppm of $\delta^{50}Cr$ mass-dependent isotope fractionation will result in an excess of 3.6 ppm on $\varepsilon^{54}Cr$.

Fig. 8. $^{55}Mn/^{52}Cr$ versus $\varepsilon^{53}Cr$ plots for ureilitic clasts. (a) Data for feldspathic clasts (orange diamonds), MG clasts (black spheres), HT clasts (gray squares) and bulk monomict ureilites from Yamakawa et al. (2010) and Qin et al. (2010b). The blue diamonds represent clasts BSa3 and TR3, which show shock-melting features (see Electronic Annex). Isochrons are plotted for all feldspathic clasts including HT clasts (excluding BSa3 and TR3), represented by an orange line with $(^{53}Mn/^{55}Mn)_0 = (3.6 \pm 0.8) \times 10^{-6}$ and for MG clasts, represented by a black line with $(^{53}Mn/^{55}Mn)_0 = (6.8 \pm 2.0) \times 10^{-6}$. (b) Zoom-in of panel 'a', with added isochron from Yamakawa et al. (2010) and Qin et al. (2010b). We show that the isochron formed by olivine and pyroxene cores from main group ureilites is steeper than those obtained for bulk ureilites and feldspathic clasts. We suggest that isochrons from this last group represent resetting or remelting ages during an impact on the UPB, 3.8 ± 1.3 Myr after CAI formation. This age is obtained from the average of feldspathic clast ages from this work, Goodrich et al. (2010) and Bischoff et al. (2014), as well as bulk ureilite ages from Yamakawa et al. (2010) and Qin et al. (2010b) (Table 5).

mantle material, where dolomite has on average 20 wt.% MgO and $\delta^{26}Mg = -2.2‰$ (range between $-1.09‰$ and $-5.5‰$). Magnesite is more Mg-rich than dolomite with MgO = 48 wt.% and is predicted to be isotopically lighter than dolomite by ∼5% at 1000 °C (Schauble, 2011). Hence, a lower percentage of magnesite-melt is required to achieve the same offset: ∼8% magnesite for an offset of 150 ppm. Since the offset between HT clasts and feldspathic clasts is on average 300 ppm, we estimate this would require on average ∼16% of the total melt to be magnesite. This is,
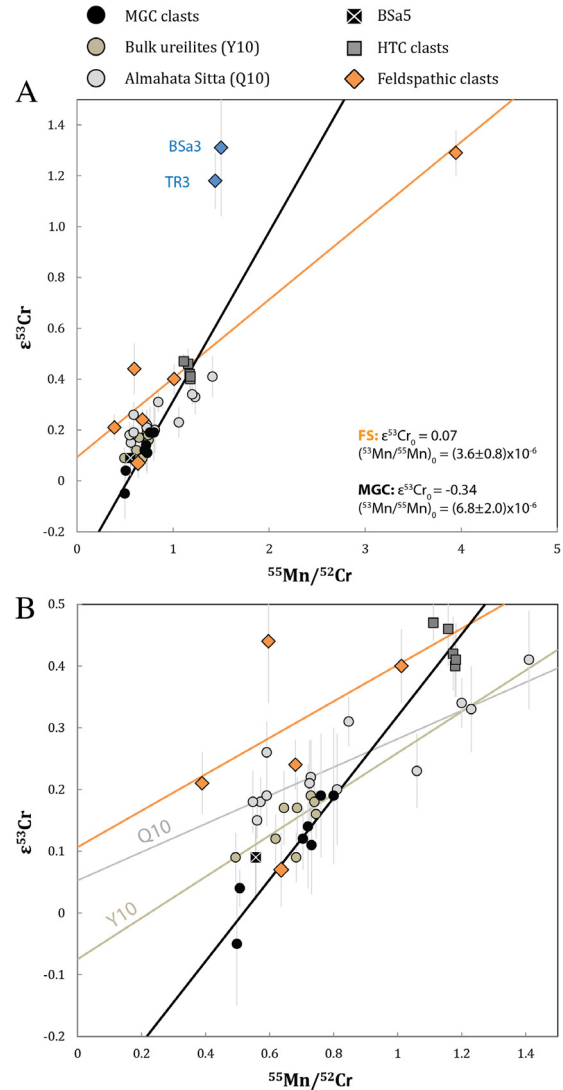
however, dependent on the equilibrium temperature and Mg-isotope composition of the magnesite.

The ^{53}Mn-^{53}Cr systematics of HT clasts agree with our suggestion that these clasts represent mantle rocks that

Table 5
Overview of ^{53}Mn-^{53}Cr and ^{26}Al-^{26}Mg isochrons and corresponding absolute ages for ureilitic clasts from this work and literature (Goodrich et al., 2010; Bischoff et al., 2014; Qin et al., 2010b; Yamakawa et al., 2010; Baker et al., 2012). All absolute ages are anchored against the D'Orbigny angrite, for which the absolute age, ^{53}Mn/^{55}Mn$_0$ and $(^{26}$Al/^{27}Al$)_0$, where taken from Amelin (2008), Glavin et al. (2004) and Schiller et al. (2015a), respectively.

	^{53}Mn/^{55}Mn$_0$	2SD	Absolute age	(+)	(−)	$(^{26}$Al/^{27}Al$)_0$	2SD	Absolute age	(+)	(−)
Feldspathic clasts	3.65E−06	1.50E−06	4564.1	1.9	2.9					
Feldspathic + HT clasts	3.62E−06	8.20E−07	4564.1	1.1	1.4					
Feldspathic clasts (G10)	2.83E−06	1.60E−07	4562.8	0.3	0.3	3.00E−07	1.10E−07	4563.2	0.5	0.4
Trachyandesite (B14)						1.10E−07	4.00E−08	4562.2	0.5	0.3
MG clasts	6.79E−06	2.00E−06	4567.5	1.4	1.9					
MG clasts + HT clasts	7.50E−06	8.30E−07	4568.1	0.6	0.6					
Almahata Sitta (Q10)	3.10E−06	1.10E−06	4563.3	1.6	2.4					
Bulk ureilites (Y10)	3.67E−06	1.00E−05	4564.3	7.1	4.3					
Leachates NWA766 (Y10)	3.35E−06	4.10E−07	4563.7	0.6	0.7					
Leachates NWA1241 (Y10)	3.50E−07	5.50E−07	<4561							
Bulk ureilites (B12)						8.80E−06	7.70E−06	4566.7	2.2	0.7

experienced multiple differentiation events, since HT clasts intersect with MG clasts as well as with feldspathic clast isochrons (Fig. 8, see also Section 5.4). Their petrological characteristics suggest that they may have initially formed as cumulates as implied from their link to Hughes type ureilites (Fig. 2), but experienced remelting at a later stage, depleting their composition in high-Ca pyroxene. Partial melts from depleted sources are in agreement with trace element compositions of feldspathic clasts (Kita et al., 2004). For a partial melt extracted from a magnesite-rich source, it is unclear whether this magnesite would have been enriched in trace elements such as Ba, U and Sr, that are normally compatible with carbonates (Ionov, 1996). Nevertheless, the Almahata Sitta trachyandesite shows enrichments in Ba, U and Sr relative to CI chondrites (Bischoff et al., 2014), which do not exclude the presence of magnesite in the source. In addition, silica-rich melts as well as alkali basalts similar to the Almahata Sitta and feldspathic clast composition are frequently associated with carbonate melts (Woolley and Kjarsgaard, 2008; Zhang et al., 2017). If indeed feldspathic clasts are melts from depleted sources represented by HT clasts during a secondary differentiation event, the presence of magnesite in cumulates required for the Mg-isotope signatures of feldspathic clasts needs to be explained. Since magnesite would be incompatible in the melt, we expect no magnesite present in cumulates formed during melting of the ureilite mantle. However, if we assume a smelting model for the ureilite mantle (Goodrich et al., 1987, 2007; Warren and Kallemeyn, 1992; Walker and Grove, 1993; Singletary and Grove, 2003), CO and CO_2 gases released during smelting will react with forsterite and water to form magnesite (Kelemen et al., 2011) in the upper 5 km of the ureilite mantle (Fig. 9). The presence of water in this reaction increases the carbonation, but is not required to form magnesite (Dabirian et al., 2012). Nevertheless, some authors argue for the presence of water on the UPB (Goodrich et al., 2015).

5.1.3. Disequilibrium isotope fractionation

Mass-dependent Mg-isotope variations as seen in feldspathic clasts can also be the result of disequilibrium isotope fractionation during magmatic processes. For example,
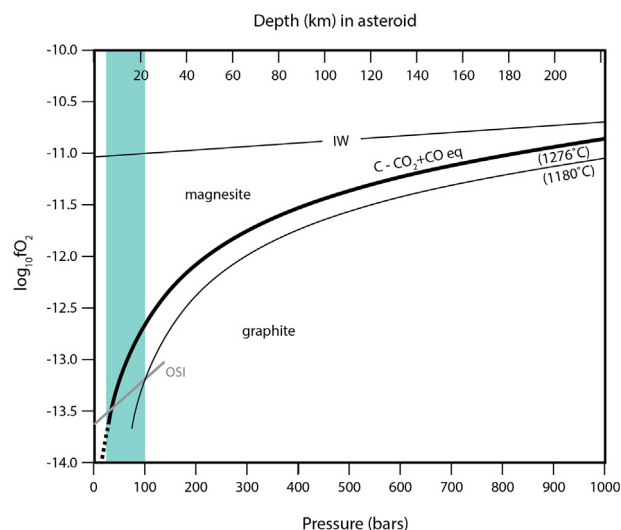

Fig. 9. Plot modified after Goodrich et al. (2013) showing oxygen fugacity in log units ($\log_{10}fO_2$) against pressure (bars). The curved lines represent C—CO + CO_2 phase equilibria at various temperatures, where the solid line reflects the transition of graphite to oxidized carbon at 1276 °C, the modeled peak temperature for bulk ureilites (Goodrich et al., 2007). The shape of these curved lines is dependent on the size of the UPB. In this figure we have included the curve with a UPB radius of 225 km. Note that different radii, with or without core do not influence the range of the CO + CO_2 stability field (Goodrich et al., 2013). Also shown, is the olivine-silica-iron equilibration line (OSI) for monomict ureilites at various $\log_{10}fO_2$ and pressure, as well as the iron-wüstite buffer (IW) for reference. The green bar represents the modeled pressure range at which monomict ureilites equilibrated. This bar is extended to greater depth when including chromite-bearing monomict ureilites (Goodrich et al., 2013).

large μ^{25}Mg differences are observed for thermal (Soret) diffusion in silicate melts, which are caused by temperature differences in magma chambers as small as 50 °C (Richter et al., 2008; Huang et al., 2010). However, we can rule this process out, since feldspathic melts will likely be enriched in heavy magnesium at the 'cold end' of the melt spectrum. Alternatively, slow Mg diffusion in solids cause melts to

be enriched in the light isotopes (Richter et al., 2008; Richter et al., 2009) and result in significantly larger Mg-isotope fractionation than observed from equilibrium fractionation. For example, Xiao et al. (2013) find $\mu^{25}Mg$ differences of ~200 ppm between olivine and orthopyroxene in lherzolites, caused by consumption of orthopyroxene that is replaced by clinopyroxene during melting. Disequilibrium fractional melting was previously suggested to explain REE patterns in ureilites (Goodrich et al., 2007). However, Barrat et al. (2016b) propose from a lithophile trace element study of ureilites that disequilibrium melting is unlikely. Furthermore, both our Mg and Cr mass-dependent isotope data support equilibrium isotope effects for HT clasts (see Section 4.2.2 and 4.3.2).

5.2. Implications for mass-dependent Cr-isotope fractionation

In addition to a mass-dependent Mg-isotope offset, a significant difference in $\delta^{50}Cr$ of 190 ppm exists between lighter HT and heavier MG clasts. We considered equilibrium isotope fractionation by melting in the presence of magnesite as a viable mechanism to create HT clasts heavy in Mg-isotopes. Due to the lack of Cr incorporation in magnesite, this process does not affect Cr-isotope fractionation. However, in agreement with the isotopically light HT clasts, equilibrium isotope fractionation will enrich the melt in heavy Cr-isotopes during partial melting, whereas the residue/cumulate is isotopically light (Moynier et al., 2011). The magnitude of mass-dependent Cr-isotope fractionation is most likely controlled by the oxidation states of Cr (Schönberg et al., 2008; Schönberg et al., 2016). For example, the amount of fractionation observed in terrestrial mantle and crust derived rocks is <0.2‰/amu (Schönberg et al., 2016), which is larger than the mass-dependent isotope variation observed between ureilite mantle residues even though the variability in oxidation states of Earth's mantle is thought to be significantly lower than that of the ureilite mantle (Papike et al., 2005; Goodrich et al., 2013; Bonnand et al., 2016). Hence, the amount of mass-dependent isotope fractionation between MG and HT clasts can be explained by differences in oxidation states within the ureilite mantle.

Collectively, the combined Mg and Cr mass-dependent isotope data suggest that equilibrium fractionation is the most likely mechanism involved in the differentiation of HT clasts, which will be summarized below. As we discuss in Section 5.1, two processes can result in a light $\mu^{25}Mg$ composition for feldspathic clasts (1) equilibrium fractionation by melting a magnesite component that is isotopically light and (2) disequilibrium isotope fractionation between residue/cumulate and partial melt. If HT clasts represent cumulates of a partial melt from main group ureilites, which has been inferred based on the Mn/Mg relationship between HT clasts and Hughes type ureilites (Downes et al., 2008), equilibrium fractionation will result in a melt with isotopically heavy Cr- and Mg-isotope compositions relative to the cumulates (Schauble, 2011). Kinetic isotope fractionation, however, will result in heavy Cr- and Mg-isotope compositions for the HT clasts relative to the melt. We find that the HT clasts have high $\delta^{50}Cr$ as well as $\mu^{25}Mg$ values, which we interpret as reflecting extraction of the

feldspathic melt in the presence of oxidized carbon (i.e., magnesite) during equilibrium isotope fractionation.

5.3. Source of the ^{54}Cr heterogeneity in the ureilite parent body

If the variability in $\varepsilon^{54}Cr$-isotope compositions is the result of equilibrium isotope fractionation, we expect an increase of $\varepsilon^{54}Cr$ correlated with a decrease of $\delta^{50}Cr$ (Fig. 7b). Hence, MG clasts with lower $\delta^{50}Cr$ values should be depleted in ^{54}Cr relative to HT clasts. In contrast, we find an opposite trend, suggesting that the $\varepsilon^{54}Cr$ variation in ureilitic clasts is unrelated to mass-dependent isotope fractionation processes. The presence of variable mass-independent ^{54}Cr abundances in meteorites and their components have been linked to different accretion regions in the protoplanetary disk (Trinquier et al., 2007, 2009; Larsen et al., 2011; Olsen et al., 2016). In particular, carbonaceous chondrites have variable, positive $\varepsilon^{54}Cr$ values with respect to terrestrial planets. On a planetesimal scale, $\varepsilon^{54}Cr$ values of distinct bulk Solar System objects are fairly constant, whereas individual components of primitive meteorites (e.g., chondrules, the potential building blocks of planets, Johansen et al., 2015) can exhibit large variations in $\varepsilon^{54}Cr$ (Van Kooten et al., 2016; Olsen et al., 2016). Differentiation on planetary bodies such as the UPB can homogenize initial isotopic heterogeneity present in its precursor material. Oxygen isotope signatures from ureilite mantle material still exhibit large mass-independent isotope variability with a total range of ~2‰ on the $\Delta^{17}O$ (Clayton and Mayeda, 1988), suggesting that initial heterogeneity of oxygen isotopes was not erased during parent body processes on the UPB. Similarly, the range in $\varepsilon^{54}Cr$ values measured in HT and MG clasts ($\Delta\varepsilon^{54}Cr_{max}$ = ~65 ppm), as well as the more variable feldspathic clasts, may also represent primordial ^{54}Cr heterogeneity. However, Cr in olivine diffuses faster than oxygen by at least two orders of magnitude at similar temperatures and oxygen fugacities (Ryerson et al., 1989; Dohmen et al., 2002; Ito and Ganguly, 2006; Chakraborty, 2010) and is, thus, much more susceptible to isotopic homogenization than oxygen. Hence, preserving isotope heterogeneity of ^{54}Cr in the ureilite mantle during its differentiation may prove more difficult than maintaining oxygen isotope heterogeneity. A potentially more viable mechanism to create ^{54}Cr variability between different ureilite mantle clasts is late admixing of ^{54}Cr-rich material to the upper ureilite mantle, perhaps via impacts of material similar to carbonaceous chondrites. This would likely affect impact-derived melts to a larger degree, thereby explaining the ^{54}Cr enrichments in HT and feldspathic clasts relative to MG clasts. The addition of carbonaceous chondrite material to the UPB can potentially explain several other features of monomict and polymict ureilites outlined in Section 5.6.

5.4. Chronological significance of ^{53}Mn-^{53}Cr data

5.4.1. ^{53}Mn-^{53}Cr data

To investigate the potential chronological relationships between individual ureilite components, we plot $\varepsilon^{53}Cr$

versus $^{55}Mn/^{52}Cr$ values for ureilites (Fig. 8), where we compare HT, MG and feldspathic clasts to Almahata Sitta ureilite fragments (Qin et al., 2010b) and bulk monomict ureilites (Yamakawa et al., 2010). Isochron data referred to in this section can be found in Table 5. Here, all calculated absolute ages are anchored to the D'Orbigny angrite with an absolute age of 4563.59 ± 0.20 Ma (Amelin, 2008) and a $(^{53}Mn/^{55}Mn)_0$ ratio of $(3.24 \pm 0.04) \times 10^{-6}$ (Glavin et al., 2004). MG clasts represent sampled olivine and pyroxene cores similar to main group ureilite compositions. Seven MG clasts form an isochron with $(^{53}Mn/^{55}Mn)_0 = (6.79 \pm 2.00) \times 10^{-6}$, corresponding to an absolute age of $4567.5^{+1.4}_{-1.9}$ Ma and within error of the timing of CV CAI formation at 4567.3 ± 0.16 Ma (Connelly et al., 2012). Extrapolation of this slope shows that HT clasts fall on the MG clast isochron. A combined isochron of HT and MG clasts results in a $(^{53}Mn/^{55}Mn)_0$ of $(7.50 \pm 0.83) \times 10^{-6}$, corresponding to an absolute age of $4568.1^{+0.6}_{-0.6}$ Ma. The $^{53}Mn-^{53}Cr$ ages obtained for MG clasts are in agreement with $^{26}Al-^{26}Mg$ ages for bulk monomict ureilites (Baker et al., 2012), with an absolute age of $4566.7^{+2.2}_{-0.7}$ Ma when tied to the D'Orbigny angrite (Schiller et al., 2015a, see also Section 5.5 for further discussion). These ages are significantly older than $^{53}Mn-^{53}Cr$ ages obtained for bulk ureilites (Qin et al., 2010b; Yamakawa et al., 2010; Fig. 8, Table 5). However, ages from Qin et al. (2010b) and Yamakawa et al. (2010) are in good agreement with the isochron for our feldspathic clasts (excluding BSa3 and TR3, see also Section 4.3.3), that corresponds to $(^{53}Mn/^{55}Mn)_0 = (3.65 \pm 1.5) \times 10^{-6}$ and an absolute age of $4564.1^{+1.9}_{-2.9}$ Ma. HT clasts also fall on the feldspathic clast isochron and when included yield $(^{53}Mn/^{55}Mn)_0 = (3.62 \pm 0.82) \times 10^{-6}$. The feldspathic isochron is in agreement with $^{53}Mn-^{53}Cr$ ages from in situ isotope analyses by secondary ionization mass spectroscopy (SIMS) on feldspathic clasts from polymict ureilites (Kita et al., 2004; Goodrich et al., 2010), the $^{26}Al-^{26}Mg$ age of the Almahata Sitta trachyandesite (Bischoff et al., 2014) and $^{182}Hf-^{182}W$ ages of bulk monomict ureilites (Budde et al., 2015). However, the $^{182}Hf-^{182}W$ age is not directly comparable to other ages, since it represents (1) a model age and (2) it discards six datapoints that when included would result in an age comparable to MG clasts and monomict ureilites (Baker et al., 2012). Budde et al. (2015) argue to discard these points based on contamination from terrestrial weathering, causing increased Hf/W ratios and ^{182}W abundances. However, three out of six 'contaminated' ureilites have similar Hf concentrations as 'uncontaminated' ureilites and have Ir/W ratios within the typical range of ureilites. Including these datapoints yields an age within error of CAI formation, which is in agreement with Baker et al. (2012) and our ages for monomict ureilites. Thus, we disregard the conclusions of Budde et al. (2015) in our discussion. Finally, the scatter of feldspathic clasts in $\varepsilon^{53}Cr$ versus $^{55}Mn/^{52}Cr$ space suggests that (1) not all feldspathic clasts were derived during the same event, (2) feldspathic clasts were not derived from the same source, or (3) $^{53}Mn-^{53}Cr$ systematics of the clasts were disturbed.

Although we cannot confidently rule out any of these possibilities at this time apart from clasts BSa3, TR3 and possibly RT3 (see Electronic Annex), feldspathic clast textures show no signs of secondary processes such as shock melting or terrestrial weathering. Furthermore, the distribution feldspathic clasts in $^{53}Mn-^{53}Cr$ and $^{26}Al-^{26}Mg$ space excludes the formation of feldspathic clasts from a single source (MG clasts or HT clasts) at different times, but may involve these clasts originating from multiple sources at the same time or over a period of time (Figs. 4 and 8).

5.4.2. The age dichotomy explained

The picture emerging from our new chronological data and other work (Yamakawa et al., 2010; Qin et al., 2010b; Goodrich et al., 2010; Bischoff et al., 2014) shows a dichotomy in age populations with separate events dated at 4567.1 ± 1.1 Ma and 4563.5 ± 1.5 Ma (Fig. 10). This raises the question if this age difference is real or an artefact related to using different dating techniques in different laboratories. Feldspathic clasts have been dated with at least four different techniques (e.g., $^{53}Mn-^{53}Cr$ and $^{26}Al-^{26}Mg$ systematics by SIMS, MC-ICPMS and TIMS) and yield consistent ages averaging to 4563.1 ± 1.6 (2SD) and, therefore, must represent a real geological event. To better understand the significance of the age dichotomy, we investigate below the type of materials sampled as well as the petrological history of these materials with respect to diffusion of elements relevant for dating techniques. Olivine grains from monomict ureilites contain highly reduced magnesian metal-bearing rims that were suggested to be formed by reactions between hot olivine and graphite, likely during rapid decompression from an impact-related event (Takeda, 1987). Hence, these reduction rims represent thermal overprinting of the differentiation event that formed the ureilite residues, resulting in a potential resetting of short-lived chronometers during the lifetime of the parent radionuclide. Thus, by sampling the cores of olivines and pyroxenes rather than bulk monomict ureilites, it is more likely that the age obtained represents the actual differentiation event that formed these residues and possibly also the ureilite core (Barrat et al., 2015) rather than later resetting. The $^{53}Mn-^{53}Cr$ ages of bulk monomict ureilites, however, include these reduction rims (Yamakawa et al., 2010; Qin et al., 2010b) that were formed while ^{53}Mn with a half-life of 3.7 Myr was still extant. Ito and Ganguly (2006) show that diffusion of Cr in olivine, using pallasites as an example, can reset the $^{53}Mn-^{53}Cr$ ages of meteorites. If the ages obtained by Yamakawa et al. (2010) and Qin et al. (2010b) indeed record the resetting ages of monomict ureilites, then this event would not likely have had an impact on the $^{26}Al-^{26}Mg$ systematics of the bulk rocks, since (1) virtually all Al was extracted from ureilite residues during partial melting and (2) at that time no ^{26}Al was present when assuming an initial $(^{26}Al/^{27}Al)_0$ similar to the angrite parent body (Schiller et al., 2015a). Hence, we suggest that the $^{26}Al-^{26}Mg$ age of 0.6 Myr after CAI formation by Baker et al. (2012) for bulk ureilites is more robust and likely records the timing of differentiation for monomict ureilite residues.

5.5. Modeling of ureilite differentiation events using initial $\mu^{26}Mg^*$ compositions

Modeling the $\mu^{26}Mg^*$ evolution of asteroidal bodies requires knowledge of the initial abundance and distribution of ^{26}Al in the solar protoplanetary disk. Although the canonical $^{26}Al/^{27}Al$ of 5.25×10^{-5} observed in CV CAIs is typically assumed to represent the initial ^{26}Al abundance of the Solar System as a whole, a number of recent studies have challenged this assumption (Larsen et al., 2011, 2016b; Schiller et al., 2015a,b; Van Kooten et al., 2016). In particular, Schiller et al. (2015a) conducted a careful comparison the ^{26}Al-^{26}Mg and U-corrected Pb-Pb dates of rapidly-cooled angrite meteorites to determine the initial $^{26}Al/^{27}Al$ ratio of inner Solar System solids. Their results establish that the initial $^{26}Al/^{27}Al$ ratio of inner Solar System reservoirs may have been reduced relative to the canonical value, a framework that we adopt in the current study (see Connelly et al. (2017) for further discussion). Correlated variability of $^{26}Mg^*$ and ^{54}Cr between bulk Solar System materials is thought to be the result of preferential destruction by thermal processing in the protoplanetary disk of labile ^{54}Cr- and ^{26}Al-rich carriers (Trinquier et al., 2009; Larsen et al., 2011; Paton et al., 2013; Schiller et al., 2015b; Van Kooten et al., 2016). Hence, ^{54}Cr compositions of inner Solar System objects can be used as a proxy to approximate their initial $^{26}Al/^{27}Al$ ratios. Ureilites have the lowest ^{54}Cr compositions observed in bulk planetary materials (Trinquier et al., 2007; Qin et al., 2010a,b; Yamakawa et al., 2010) and are therefore thought to have a corresponding low initial bulk $^{26}Al/^{27}Al$ ratio. Due to the lack of representative bulk ureilite materials it is not possible to derive a robust estimate of the initial $^{26}Al/^{27}Al$ ratio of the UPB. Rather, we use the angrite parent body with $\varepsilon^{54}Cr = -0.36 \pm 0.07$ (Trinquier et al., 2007) for which the initial bulk $^{26}Al/^{27}Al$ ratio is calculated to be $1.33^{+0.21}_{-0.18} \times 10^{-5}$ (Schiller et al., 2015a) to provide an upper limit on the initial ^{26}Al abundance of the UPB. We model the evolution of the bulk UPB (Fig. 11) assuming an upper limit initial $^{26}Al/^{27}Al$ ratio of $1.33^{+0.21}_{-0.18} \times 10^{-5}$ (Schiller et al., 2015a), a solar $^{27}Al/^{24}Mg$ ratio of 0.09781 $\pm$ 0.00029 (Paton et al., 2012) and an initial $\mu^{26}Mg^*$ of -15.9 ppm (Larsen et al., 2011). This results in a maximum $\mu^{26}Mg^*$ ingrowth of up to -6 ppm for the bulk UPB (Fig. 11).

Main Group clasts, similarly to monomict ureilites, have an average $\mu^{26}Mg^*$ of -10.6 ± 5.3 ppm, and our model ages suggest that these melt residues formed approximately 0.7 Myr after $t = 0$ (CV CAI formation; Connelly et al., 2012). We note that using an initial $^{26}Al/^{27}Al$ ratio of $(1.08 \pm 0.29) \times 10^{-5}$ for the bulk UPB as suggested by Larsen et al. (2011) yields a slightly younger age for ureilite residues of 0.9 Myr (Fig. 11, dotted line), but still within the age range of MG clasts and monomict ureilites (Baker et al., 2012). Alternatively, using a canonical $^{26}Al/^{27}Al$ ratio requires extremely rapid accretion and differentiation of the UPB at $t = 0$.

Hughes Type clasts either represent mantle residues or cumulates related to partial melting in the ureilite mantle.
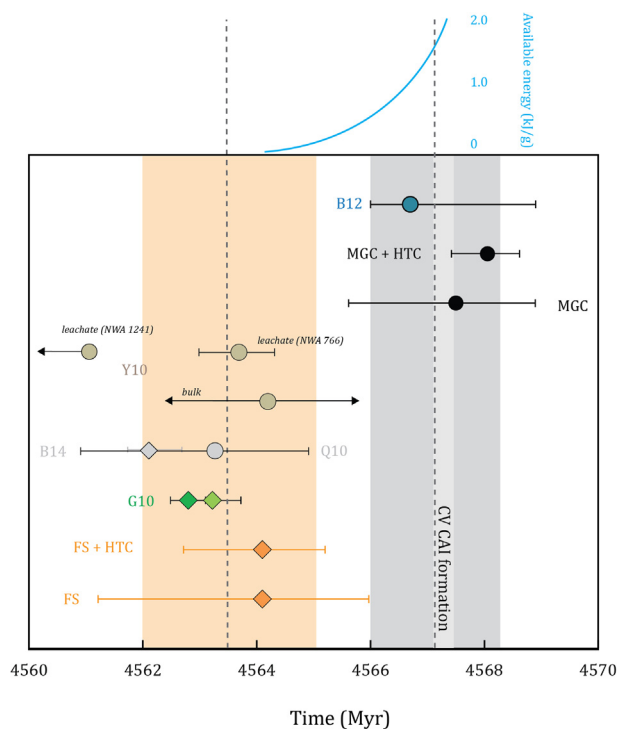

Fig. 10. Ages relative to CV CAI formation (Connelly et al., 2012) for MG olivine and pyroxene cores (black spheres: ^{53}Mn-^{53}Cr ages, see Table 5) and the bulk monomict ureilite ^{26}Al-^{26}Mg age by Baker et al. (2012) (B12, blue sphere). The average of these ages with a 2SD error is represented by the dark gray box. The yellow box represents the average age of feldspathic clasts in this work (dark orange diamonds: ^{53}Mn-^{53}Cr ages, see Table 5), feldspathic clasts measured by Goodrich et al. (2010) (green diamonds, G10), bulk ureilites from Almahata Sitta (Q10, gray sphere; Qin et al., 2010b), ALM-A trachyandesite (B14, gray diamond; Bischoff et al., 2014) and bulk main group ureilites and leachates thereof by Yamakawa et al. (2010) (brown spheres, Y10). The top panel in the figure depicts available energy from the decay of ^{26}Al with time, where $(^{26}Al/^{27}Al)_0$ and the Al abundance is equal to the angrite parent body (Schiller et al., 2015a). We show that the differentiation event constrained by the yellow box cannot be initiated by decay of ^{26}Al.

These clasts show mixed petrological characteristics that could argue for them being residual or cumulate lithologies (Section 5.1.2). Moreover, ^{53}Mn-^{53}Cr systematics of these clasts show that they can be placed on the MG clast as well as the feldspathic isochron (Fig. 8). Hence, HT clasts may be representative of multiple differentiation events. Modeling the $\mu^{26}Mg^*$ evolution of the bulk UPB shows that HT clasts must have formed primarily as cumulates, since a residue origin requires a $\mu^{26}Mg^* < -6$ ppm. Treating HT clasts firstly as cumulates, the Al/Mg ratio of the initial melt from which they crystallized is unknown, but can be modeled as a 25% partial melt from the bulk UPB. The Al/Mg ratio of the initial melt was calculated with the PELE software (Boudreau, 1999), a Windows version of MELTS. We used temperature ($T = 1050$–$1250\,°C$), pressure ($P = 100$ bar, isobaric) and oxygen fugacity ($fO_2 = -13.8$) input parameters from Goodrich et al. (2007) and an initial bulk composition similar to ordinary chondrites. In earlier
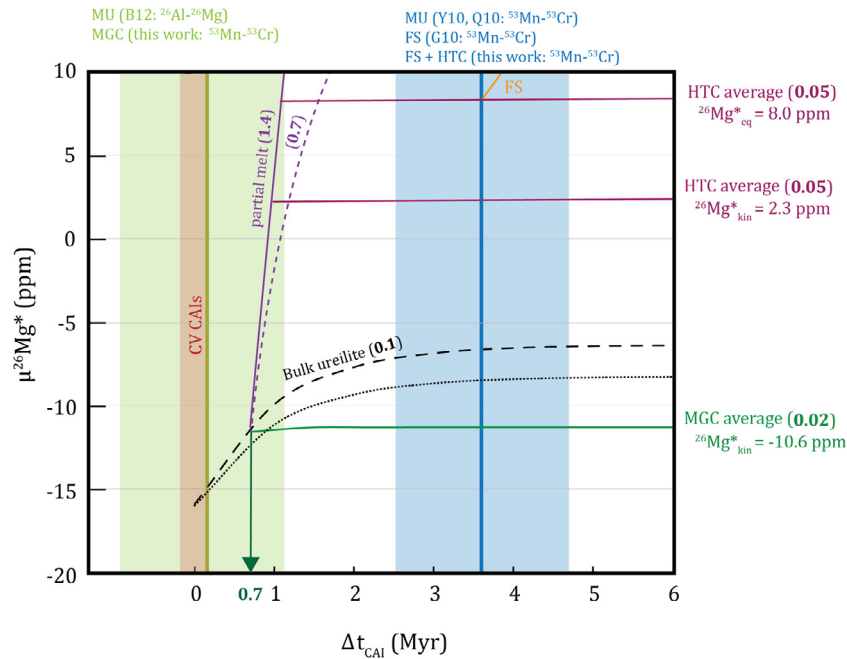
Fig. 11. Plot depicting radiogenic ingrowth of ^{26}Mg* with time after CAI formation ($t = 0$ at 4567.3 Ma; Connelly et al., 2012). The initial ^{26}Al/^{27}Al composition of the UPB is assumed to be similar to the angrite parent body with $(^{26}$Al/^{27}Al$)_0 = 1.33^{+0.21}_{-0.18} \times 10^{-5}$ (dashed black line, Schiller et al., 2015a), whereas the Al/Mg ratio is solar (Al/Mg = 0.1). Also shown is the evolution of the UPB with $(^{26}$Al/^{27}Al$)_0 = (1.08 \pm 0.29) \times 10^{-5}$ (dotted line, Larsen et al., 2011). We obtain a model age of ~0.7 Myr after $t = 0$, for the timing of differentiation of MG clasts representing mantle residues. This model age is calculated from the Al/Mg ratio (0.02) and corresponding average μ^{26}Mg* value of MG clasts (green line) and is similar to the ^{26}Al-^{26}Mg age from Baker et al. (2012) for monomict ureilites. Since the error on the average μ^{26}Mg* value of MG clasts is 5.3 ppm (2SD), the error on the modeled absolute age is large. We note, however, that the ^{53}Mn-^{53}Cr age for MG clasts gives an additional constraint for the Al-Mg model ages. The green box represents the average age for the first differentiation event from Fig. 10, whereas the blue box represents the average age for the second differentiation event. Also modeled, is a partial melt derived from ureilite residues 0.7 Myr after CAI formation, with a modeled Al/Mg ratio of 0.7 (dashed purple line, fractional crystallization) and 1.4 (solid purple line, equilibrium fractionation). Within this range of Al/Mg ratios and modeled for HT clasts μ^{26}Mg* values corrected for equilibrium or kinetic law, cumulates differentiated within ~0.8 Myr years of partial melt extraction from the UPB (red lines). Feldspathic melts derived from HT clasts compositions ~3.8 Myr after CAI formation (orange line), agree with observed μ^{26}Mg* values for feldspathic clasts.

models, carbonaceous chondrites (CI, CM, CV) with Ca/Al = 2.5* CI are typically used as the precursor material to the UPB. This is based on the high carbon content in monomict ureilites and the oxygen isotope data corresponding to a slope ~1 CCAM line (Kita et al., 2004; Goodrich et al., 2007). However, Cr, Ca, O and Tm isotope data essentially precludes that ureilites were derived from carbonaceous chondrites (Trinquier et al., 2007; Qin et al., 2010b; Yamakawa et al., 2010; Warren, 2011; Schiller et al., 2015b; Barrat et al., 2016a). Additionally, the effect of basalt removal on MgO-SiO$_2$ and FeO-SiO$_2$ relationships suggests a non-carbonaceous origin for ureilites (Warren, 2011). Hence, in our model we use ordinary chondrites as precursor material to the UPB. A modeled 25% partial melt from an ordinary chondrite bulk composition yields Al/Mg ratios between 0.7 and 1.4, for fractional and equilibrium crystallization, respectively. In Fig. 11, we show the modeled μ^{26}Mg* evolution of the range of partial melts and derivative cumulates with μ^{26}Mg* values of 2.3 ± 6.3 ppm or 8.0 ± 5.0 ppm, assuming either kinetic or equilibrium processes during the mass-dependent isotope fractionation, respectively. The resulting differentiation age of HT clasts cumulates is then 0.9–1.5 Myr after CAI formation. It is apparent from Fig. 11 that HT clasts can-

not have formed as primary residues from the bulk UPB, since this would have resulted in μ^{26}Mg* < −6 ppm. However, a second melting event involving HT clasts cumulates around 3.8 Myr after CAI formation can result in the olivine-rich, low-Ca compositions observed for HT clasts and produce the μ^{26}Mg* values measured in feldspathic clasts. This model agrees with the notion that feldspathic clasts are derived from depleted sources, based on their trace element and REE patterns (Kita et al., 2004). A late melting event, required to produce feldspathic clasts, cannot be initiated by heating from the decay of ^{26}Al as shown by the decay curve with $(^{26}$Al/^{27}Al$)_0 = 1.33 \times 10^{-5}$ in Fig. 10: at 3.5 Myr after $t = 0$, virtually no ^{26}Al remains and the parent body cools. Hence, this event requires an alternative heating mechanism, possibly by major impact (s). We note that a disruptive impact to the UPB is thought to be prerequisite to the formation of reduction rims in monomict ureilite olivines (Takeda, 1987).

5.6. Disruption of the ureilite parent body

Polymict ureilites are breccias containing clasts that are derived from various depths in the ureilite mantle. This suggests that these meteorites accreted after a major disruptive

event able to exhume materials from tens of kilometers deep. Such a large disruptive impact event is expected to leave its mark on the geological record of the UPB, for example in the form of shock or decompression melting. Late stage melting, 3.8 ± 1.3 Myr after CAI formation, is best explained by impact heating, since essentially no ^{26}Al is left for heating by radioactive decay (Fig. 10). Furthermore, the high amount of carbon in ureilites, the $\delta^{15}N$ isotope anomalies, enrichment in noble gases and grain lineation in ureilites have been attributed to an impact event (Warren and Kallemeyn, 1988; Rubin, 1988; Warren and Rubin, 2010; Day et al., 2017), although the carbon abundance in ureilites is more likely to be the result of a magmatic process (Rubin, 1988). The relative enrichment of ^{15}N is only found in polymict ureilites, suggesting that the impact projectile was carbonaceous in nature (Grady and Pillinger, 1988) in contrast to the non-carbonaceous UPB. While the impactor that is invoked to have exhumed the monomict ureilites and the impactor that would have caused impact melting do not necessarily have to represent the same event, the data at hand does not exclude the possibility that the exhumation and melting are related to the same impact event. In this scenario, an impactor can exhume material from kilometers deep, while at the same time causing decompression melting in shallow source cumulates. Ureilite material ejected during the impact may then have accreted back to the surface and subsequently mixed with newly formed feldspathic clasts forming a polymict breccia.

The $\varepsilon^{54}Cr$ and $\mu^{26}Mg^*$ values of various chondritic clasts in DaG319 exclude these materials as precursors to the

UPB. However, based on the high abundance of dark clasts in the breccias relative to other chondritic clasts (i.e., R, CB, EC and OC), we speculate that the dark clasts may be derived from the proposed large impactor. As mentioned before, these dark clasts are very similar in $\mu^{26}Mg^*$ and $\varepsilon^{54}Cr$ isotope composition to CI carbonaceous chondrites. However, their position in $\varepsilon^{53}Cr$ versus $\varepsilon^{54}Cr$ space (Fig. 12) suggests that these clasts have experienced less thermal processing than CI chondrites and, thus, are more pristine. The primitive nature of these dark clasts suggests that their parent body may have accreted at a greater heliocentric distance compared to other carbonaceous chondrites. Hence, the inward migration of a larger asteroidal body with a primitive carbonaceous chondrite composition may reflect an epoch of disruption in the outer Solar System (Johnson et al., 2016). Indeed, the volatile-rich dark clasts in our study proposed to be fragments of a carbonaceous impactor are found in abundance in other meteorite breccias as well (Bischoff et al., 2006). A study of these objects might give insights into the flux of volatile-rich asteroid bodies from the outer Solar System to the accretion region of the terrestrial planets. Dark clasts as well as impact related lithologies from planetary bodies may have the potential to place constraints on astrophysical models representing the dynamical evolution of our Solar System.

6. CONCLUSIONS

We studied the petrology and chemistry as well as the Mg- and Cr-isotope systematics of ureilitic clasts from the polymict ureilite DaG 319. Our data provides the following
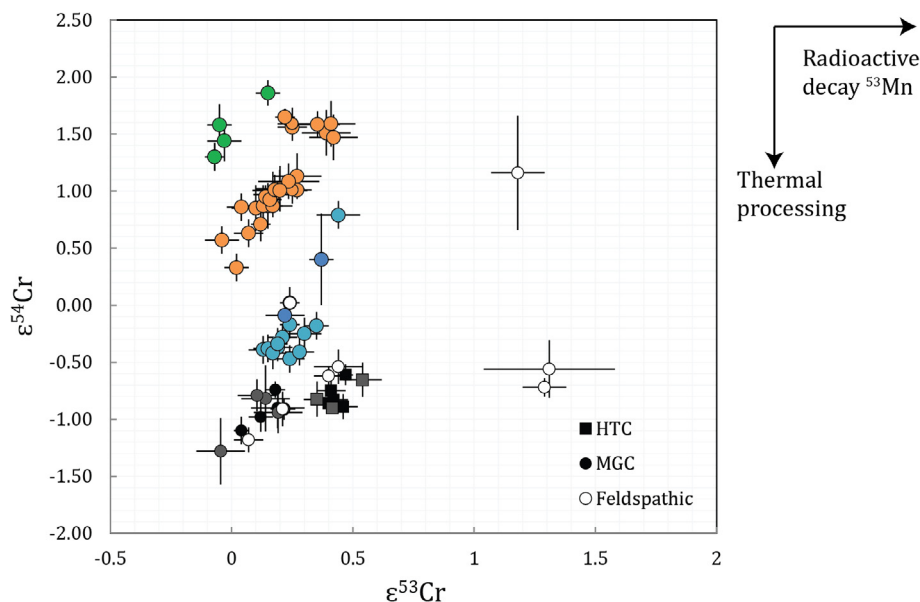

Fig. 12. Plots of $\varepsilon^{53}Cr$ versus $\varepsilon^{54}Cr$. Data for carbonaceous chondrites (orange) (Trinquier et al., 2007, 2009; Shukolyukov and Lugmair, 2006; Qin et al., 2010a; Van Kooten et al., 2016; Göpel et al., 2015), ordinary chondrite data (light blue) (Trinquier et al., 2007, 2009; Qin et al., 2010a), dark clasts in DaG 319 from this study (green), chondrule-containing clasts from this study (dark blue) and ureilite clasts from this study, where black represents data from TIMS and gray from MC-ICPMS. Variations in $\varepsilon^{54}Cr$ between bulk Solar System materials can be attributed to thermal processing of ^{54}Cr-rich dust (Trinquier et al., 2009), whereas unidirectional changes in $\varepsilon^{53}Cr$ correspond to decay from ^{53}Mn to ^{53}Cr as seen for feldspathic and HT clasts.

constraints on the melting and differentiation history of the UPB:

(1) The DaG 319 polymict ureilite consists foremost of MG clasts related to monomict ureilites with varying Mg#s (0.74–0.91), as well as a large fraction of olivine-orthopyroxene (HT) clasts with consistently high Mg#s (0.89). Based on petrological and mineralogical characteristics, MG clasts are residues, wheras HT clasts were primarily formed as cumulates and further partial melting. A third type of clasts is recognized in DaG 319, consisting of feldspathic clasts that represent partial melts from the ureilite mantle.

(2) Significant mass-dependent Mg-isotope fractionation is present between feldspathic clasts and clasts related to ureilitic mantle residues and cumulates ($\Delta\mu^{25}Mg = 450$ ppm), which can best be explained by equilibrium isotope fractionation during melting including a magnesite component enriching the melt in light Mg-isotopes. We suggest that Mg-carbonates were stable in the upper ureilite mantle, whereas pure carbon phases such as graphite were stable at higher pressures and depths. This is in agreement with a lack of carbon-related phases in HT clasts, whereas MG clasts contain affluent carbon.

(3) The timing of the differentiation events leading to the formation of MG and HT clasts are constrained by ^{53}Mn-^{53}Cr systematics and ^{26}Al-^{26}Mg model ages, which show that a primary differentiation event resulting in the formation of main group ureilite residues and related to decay of ^{26}Al occurred early, ~0.7 Myr after CAI formation. We suggest that a later (~3.8 Myr after $t = 0$) major disruptive impact was responsible for remelting of HT clasts, formation of feldspathic melts and resetting of ^{53}Mn-^{53}Cr ages for monomict ureilites. These feldspathic melts may have been extracted from multiple sources throughout the UPB.

(4) The MG clasts and HT clasts show variable ε^{54}Cr values that are unrelated to mass-dependent Cr-isotope fractionation. We propose that the variations in ε^{54}Cr are the result of admixing of carbonaceous chondritic matter during an impact-related disruptive event that caused late-stage melting in the upper ureilite mantle ~3.8 Myr after CAI formation. The impactor may be represented by pristine dark clasts found in DaG 319.

ACKNOWLEDGMENTS

APPENDIX A. SUPPLEMENTARY MATERIAL

Supplementary data associated with this article can be found, in the online version, at http://dx.doi.org/10.1016/j.gca.2017.03.033.

REFERENCES

Amelin Y. (2008) U-Pb ages of angrites. *Geochim. Cosmochim. Acta* **72**, 221–232.

Amelin, Y., Koefoed, P., Bischoff, A., Budde, G., Brennecka, G. and Kleine, T. (2015). Pb isotopic age of ALM-A - a feldspar-rich volcanic rock from the crust of the ureilite parent body. In: 78th Annual Meeting on Meteorological Society, p. 5344.

Baker J. A., Schiller M. and Bizzarro M. (2012) ^{26}Al-^{26}Mg deficit dating ultramafic meteorites and silicate planetesimal differentiation in the early Solar System? Geochim. *Cosmochim. Acta* **77**, 415–531.

Barrat J., Dauphas N., Gillet P., Bollinger C., Etoubleau J., Bischoff A. and Yamaguchi A. (2016a) Evidence from Tm anomalies for non-CI refractory lithophile element proportions in terrestrial planets and achondrites. *Geochim. Cosmochim. Acta* **176**, 1–17.

Barrat J.-A., Jambon A., Yamaguchi A., Bischoff A., Rouget M.-L. and Liorzou C. (2016b) Partial melting of a C-rich asteroid: Lithophile trace elements in ureilites. *Geochim. Cosmochim. Acta* **194**, 163–178.

Barrat J.-A., Rouxel O., Wang K., Moynier F., Yamaguchi A., Bischoff A. and Langlade J. (2015) Early stages of core segregation recorded by Fe isotopes in an asteroidal mantle. *Earth Planet. Sci. Letts.* **419**, 93–100.

Bast R., Scherer E. and Bischoff A. (2016) The ^{176}Lu-^{176}Hf systematics of ALM-A: a sample of the recent Almahata Sitta meteorite fall. *Geochem. Persp. Lett.* **3**, 45–54.

Bischoff A., Horstmann M., Barrat J.-A., Chaussidon M., Pack A., Herwartz D., Ward D., Vollmer C. and Decker S. (2014) Trachyandesitic volcanism in the early solar system. *Proc. Nat. Ac. Sci. USA* **111**, 12689–12692.

Bischoff A., Scott E., Metzler K. and Goodrich C. (2006) Nature and origins of meteoritic breccias. *Meteor. Early Solar System II*, 679–712.

Bizzarro M., Haack H., Baker J. and Lundgaard K. (2005) Rapid timescales for accretion and melting of differentiated planetesimals inferred from Al-Mg chronometry. *Astrophys. J.* **632**, L41–L44.

Bizzarro M., Paton C., Larsen K., Schiller M., Trinquier A. and Ulfbeck D. (2011) High-precision Mg-isotope measurements of terrestrial and extraterrestrial material by HR-MC-ICPMS-implications for the relative and absolute Mg-isotope composition of the bulk silicate Earth. *J. Anal. At. Spectrom.* **26**, 565–577.

Bonnand P., Williams H., Parkinson I., Wood B. and Halliday A. (2016) Stable chromium isotopic composition of meteorites and metal-silicate experiments: Implications for fractionation during core formation. *Earth Planet. Sci. Letts.* **435**, 14–21.

Boudreau A. (1999) PELE-a version of the MELTS software program for the PC platform. *J. Comput. Geosci.* **25**, 201–203.

Budde G., Kruijer T., Fischer-Gödde M., Irving A. and Kleine T. (2015) Planetesimal differentiation revealed by the Hf-W systematics of ureilites. *Earth Planet. Sci. Letts.* **430**, 316–325.

Chakraborty S. (2010) Diffusion Coefficients in Olivine, Wadsleyite and Ringwoodite. *Rev. Min. Geochem.* **72**, 603–639.

Clayton R. N. and Mayeda T. K. (1988) Formation of ureilites by nebular processes. *Geochim. Cosmochim. Acta* **52**, 1313–1318.

Clayton R. N. and Mayeda T. K. (1996) Oxygen isotope studies of achondrites. *Geochim. Cosmochim. Acta* **60**, 1999–2017.

Cohen B. A., Goodrich C. A. and Keil K. (2004) Feldspathic clast populations in polymict ureilites: stalking the missing basalts from the ureilite parent body. *Geochim. Cosmochim. Acta* **68**, 4249–4266.

Connelly J., Bollard J. and Bizzarro M. (2017) Pb-Pb chronometry and the early solar system. *Geochim. Cosmochim. Acta* **201**, 345–363.

Connelly J. N., Bizzarro M., Krot A. N., Nordlund A., Wielandt D. and Ivanova M. A. (2012) The absolute chronology and thermal processing of solids in the solar protoplanetary disk. *Science* **338**, 651–655.

Dabirian R., Beiranvand M. and Aghahoseini S. (2012) Mineral carbonation in peridotite rock for CO_2 sequestration and a method of leakage reduction of CO_2 in the rock. *Nafta* **63**, 44–48.

Day J. M., Corder C. A., Cartigny P., Steele A. M., Assayag N., Rumble D. and Taylor L. A. (2017) A carbon-rich region in Miller Range 091004 and implications for ureilite petrogenesis. *Geochim. Cosmochim. Acta* **379**, 379–395.

Dohmen R., Chakraborty S. and Becker H.-W. (2002) Si and O diffusion in olivine and implications for characterizing plastic flow in the mantle. *Geophys. Res. Lett.* **29**, 26-1–26-4.

Downes H., Mittlefehldt D., Kita N. and Valley J. (2008) Evidence from polymict ureilite meteorites for a disrupted and re-accreted single ureilite parent asteroid gardened by several distinct impactors. *Geochim. Cosmochim. Acta* **72**, 4825–4844.

Göbel R., Ott U. and Begemann F. (1978) On trapped noble gases in ureilites. *J. Geophys. Res.: Solid Earth* **83**, 855–867.

Glavin D., Kubny A., Jagoutz E. and Lugmair G. (2004) Mn-Cr isotope systematics of the D'Orbigny angrite. *Meteor. Planet. Sci.* **39**, 693–700.

Goodrich C., Fioretti A., Tribaudino M. and Molin G. (2001) Primary trapped melt inclusions in olivine in the olivine-augite-orthopyroxene ureilite Hughes 009. *Geochim. Cosmochim. Acta* **65**, 621–652.

Goodrich C., Sutton S., Wirick S. and Jercinovic M. (2013) Chromium valences in ureilite olivine and implications for ureilite petrogenesis. *Geochim. Cosmochim. Acta* **122**, 280–305.

Goodrich C. A. (1999) Are ureilites residues from partial melting of chondritic material? The answer from MAGPOX. *Meteor. Planet. Sci.* **34**, 109–119.

Goodrich C. A. and Delaney J. S. (2000) Fe/Mg-Fe/Mn relations of meteorites and primary heterogeneity of primitive achondrite parent bodies. *Geochim. Cosmochim. Acta* **64**, 149–160.

Goodrich C. A., Hutcheon I. D., Kita N. T., Huss G. R., Cohen B. A. and Keil K. (2010) [53]Mn-[53]Cr and [26]Al-[26]Mg ages of a feldspathic lithology in polymict ureilites. *Earth Planet. Sci. Lett.* **295**, 531–540.

Goodrich C. A., Jones J. H. and Berkley J. L. (1987) Origin and evolution of the ureilite parent magmas: multi-stage igneous activity on a large parent body. *Geochim. Cosmochim. Acta* **51**, 2255–2273.

Goodrich C. A., Orman J. A. V. and Wilson L. (2007) Fractional melting and smelting on the ureilite parent body. *Geochim. Cosmochim. Acta* **71**, 2876–2895.

Goodrich C. A., Scott E. R. D. and Fioretti A. M. (2004) Ureilitic breccias: clues to the petrologic structure and impact disruption of the ureilite parent asteroid. *Chemie der Erde - Geochem.* **64**, 283–327.

Goodrich G., Hartmann W., O'Brien D., Weidenschilling S., Wilson L., Michel P. and Jutzi M. (2015) Origin and history of ureilitic material in the solar system: the view from asteroid 2008 TC3 and the Almahata Sitta meteorite. *Meteor. Planet. Sci.* **50**, 782–809.

Göpel C., Birck J., Galy A., Barrat J.-A. and Zanda B. (2015) Mn-Cr systematics in primitive meteorites: insights from mineral separation and partial dissolution. *Geochim. Cosmochim. Acta* **156**, 1–24.

Grady M. M. and Pillinger C. T. (1988) ^{15}N-enriched nitrogen in polymict ureilites and its bearing on their formation. *Nature* **331**, 321–323.

Henderson G., Calas G. and Stebbins J. (2006) The structure of silicate glasses and melts. *Elements* **2**, 269–273.

Huang F., Chakraborty P., Lundstrom C. C., Holmden C., Glessner J. J. G., Kieffer S. W. and Lesher C. E. (2010) Isotope fractionation in silicate melts by thermal diffusion. *Nature* **464**, 396–400.

Huang F., Zhang Z., Lundstrom C. C. and Zhi X. (2011) Iron and magnesium isotopic compositions of peridotite xenoliths from Eastern China. *Geochim. Cosmochim. Acta* **75**, 3318–3334.

Ikeda Y., Kita N. T., Morishita Y. and Weisberg M. (2003) Primitive clasts in the Dar al Gani 319 polymict ureilite: precursors of the ureilites. *Antarct. Meteorite Res.* **16**, 105–127.

Ikeda Y. and Prinz M. (2001) Magmatic inclusions and felsic clasts in the Dar al Gani 319 polymict ureilite. *Meteor. Planet. Sci.* **36**, 481–499.

Ikeda Y., Prinz M. and Nehru C. (2000) Lithic and mineral clasts in the Dar al Gani 319 polymict ureilite. *Antar. Meteor. Res.* **13**, 177–221.

Ionov D. (1996) Trace element composition of mantle derived carbonates and coexisting phases in peridotite xenoliths from alkali basalts. *J. Petrol.* **39**, 1931–1941.

Ito M. and Ganguly J. (2006) Diffusion kinetics of Cr in olivine and [53]Mn-[53]Cr thermochronology of early solar system objects. *Geochim. Cosmochim. Acta* **70**, 799–809.

Johansen A., Mac Low M.-M., Lacerda P. and Bizzarro M. (2015) Growth of asteroids, planetary embryos, and Kuiper belt objects by chondrule accretion. *Sci. Adv.* **1**, 1500109.

Johnson B., Walsh K., Milton D., Krot A. and Levison H. (2016) Timing of the formation and migration of giant planets as constrained by CB chondrites. *Sci. Adv.* **2**, e1601658.

Kelemen P., Matter J., Streit E., Rudge J., Curry W. and Blusztajn J. (2011) Rates and mechanisms of mineral carbonation in peridotite: natural processes and recipes for enhanced, in situ CO_2 capture and storage. *Annu. Rev. Earth Planet. Sci.* **39**, 45–76.

Kita N. T., Goodrich C. A., Fu B., Spicuzza M. J. and Valley J. W. (2006) Oxygen isotopes in mafic and feldspathic clasts from polymict ureilites. *Meteor. Planet. Sci. Supp.* **41**, 5161.

Kita N. T., Hutcheon I. D., Huss G. R. and Goodrich C. A. (2007) [26]Al-[26]Mg and [53]Mn-[53]Cr age of a feldspathic lithology in polymict ureilites. *Ann. Meteor. Soc. Meet.* **42**, 5231.

Kita N. T., Ikeda Y., Shimoda H., Morishita Y. and Togashi S. (2003) Timing of basaltic volcanism in ureilite parent body inferred from the [26]Al ages of plagioclase-bearing clasts in DaG-319 polymict ureilite. *Lun. Planet. Sci. Conf.*, 1557.

Kita N. T., Ikeda Y., Togashi S., Liu Y., Morishita Y. and Weisberg M. K. (2004) Origin of ureilites inferred from a SIMS oxygen isotopic and trace element study of clasts in the Dar al Gani 319 polymict ureilite. *Geochim. Cosmochim. Acta* **68**, 4213–4235.

Kleine T., Hans U., Irving A. J. and Bourdon B. (2012) Chronology of the angrite parent body and implications for core formation in protoplanets. *Geochim. Cosmochim. Acta* **84**, 186–203.

Larsen K., Wielandt D., Schiller M. and Bizzarro M. (2016a) Chromatographic speciation of Cr(III)-species, inter-species equilibrium isotope fractionation and improved chemical purification strategies for high-precision isotope analysis. *J. Chrom. A* **1443**, 162–174.

Larsen K. K., Schiller M. and Bizzarro M. (2016b) Accretion timescales and style of asteroidal differentiation in an [26]Al-poor protoplanetary disk. *Geochim. Cosmochim. Acta* **176**, 295–315.

Larsen K. K., Trinquier A., Paton C., Schiller M., Wielandt D., Ivanova M., Connelly J., Nordlund A., Krot A. and Bizzarro M. (2011) Evidence for magnesium isotope heterogeneity in the solar protoplanetary disk. *Astrophys. J. Lett.* **735**, L37.

Lugmair G. W. and Shukolyukov A. (1998) Early solar system timescales according to [53]Mn-[53]Cr systematics. *Geochim. Cosmochim. Acta* **62**, 2863–2886.

Moynier F., Yin Q.-Z. and Schauble E. (2011) Isotopic evidence of Cr partitioning into Earth's core. *Science* **331**, 1417–1420.

Olsen M., Wielandt D., Schiller M., van Kooten E. and Bizzarro M. (2016) Magnesium and [54]Cr isotope compositions of carbonaceous chondrite chondrules - insights into early disk processes. *Geochim. Cosmochim. Acta* **191**, 118–138.

Papike J., Karner J. and Shearer C. (2005) Comparative planetary mineralogy: valence state partitioning of Cr, Fe, Ti, and V among crystallographic sites in olivine, pyroxene, and spinel from planetary basalts. *Am. Min.* **90**, 277–290.

Paton C., Hellstrom J., Paul B., Woodhead J. and Hergt J. (2011) Iolite: Freeware for the visualisation and processing of mass spectrometric data. *J. Anal. At. Spectrom.* **26**, 2508–2518.

Paton C., Schiller M. and Bizzarro M. (2013) Identification of an [84]Sr-depleted carrier in primitive meteorites and implications for thermal processing in the solar protoplanetary disk. *Astrophys. J.* **763**, L40.

Paton C., Schiller M., Ulfbeck D. and Bizzarro M. (2012) High-precision [27]Al/[24]Mg ratio determination using a modified isotope-dilution approach. *J. Anal. At. Spectrom.* **27**, 644–652.

Qin L., Alexander C. M. O., Carlson R. W., Horan M. F. and Yokoyama T. (2010a) Contributors to chromium isotope variation of meteorites. *Geochim. Cosmochim. Acta* **74**, 1122–1145.

Qin L., Rumble D., Alexander C. M. O., Carlson R. W., Jenniskens P. and Shaddad M. H. (2010b) The chromium isotopic composition of Almahata Sitta. *Meteor. Planet. Sci.* **45**, 1771–1777.

Rankenburg K., Humayun M., Brandon A. and Herrin J. (2008) Highly siderophile elements in ureilites. *Geochim. Cosmochim. Acta* **72**, 4642–4659.

Richter F. M., Watson E. B., Mendybaev R., Dauphas N., Georg B., Watkins J. and Valley J. (2009) Isotopic fractionation of the major elements of molten basalt by chemical and thermal diffusion. *Geochim. Cosmochim. Acta* **73**, 4250–4263.

Richter F. M., Watson E. B., Mendybaev R. A., Teng F.-Z. and Janney P. E. (2008) Magnesium isotope fractionation in silicate melts by chemical and thermal diffusion. *Geochim. Cosmochim. Acta* **72**, 206–220.

Rubin A. E. (1988) Formation of ureilites by impact-melting of carbonaceous chondritic material. *Meteoritics* **23**, 333–337.

Ryerson F. J., Durham W. B., Cherniak D. J. and Lanford W. A. (1989) Oxygen diffusion in olivine: effect of oxygen fugacity and implications for creep. *J. Geophys. Res.: Solid Earth* **94**, 4105–4118.

Sanders I., Scott E. and Delaney J. (2017) Origin of mass-independent oxygen isotope variation among ureilites: clues from chondrites and primitive achondrites. *Meteor. Planet. Sci.*, 1–19.

Sandrin A., Edfelt A., Waight T., Berggren R. and Elming S.-A. (2009) Physical properties and petrologic description of rock samples from an IOCG mineralized area in the northern Fennoscandian Shield, Sweden. *J. Geochem. Explor.* **103**, 80–96.

Schauble E. A. (2011) First-principles estimates of equilibrium magnesium isotope fractionation in silicate, oxide, carbonate and hexaaquamagnesium(2+) crystals. *Geochim. Cosmochim. Acta* **75**, 844–869.

Schiller M., Baker J., Creech J., Paton C., Millet M.-A., Irving A. and Bizzarro M. (2011) Rapid timescales for magma ocean crystallization on the howardite-eucrite-diogenite parent body. *Astrophys. J. Lett.* **740**, L22.

Schiller M., Baker J. A. and Bizzarro M. (2010) [26]Al-[26]Mg dating of asteroidal magmatism in the young Solar System. *Geochim. Cosmochim. Acta* **74**, 4844–4864.

Schiller M., Connelly J. N., Glad A. C., Mikouchi T. and Bizzarro M. (2015a) Early accretion of protoplanets inferred from a reduced inner solar system [26]Al inventory. *Earth Planet. Sci. Lett.* **420**, 45–54.

Schiller M., Dallas J., Creech J., Bizzarro M. and Baker J. (2017) Tracking the formation of magma oceans in the solar system using stable magnesium isotopes. *Geochem. Persp. Lett.* **3**, 22–31.

Schiller M., Paton C. and Bizzarro M. (2015b) Evidence for nucleosynthetic enrichment of the protosolar molecular cloud core by multiple supernova events. *Geochim. Cosmochim. Acta* **149**, 88–102.

Schiller M., Van Kooten E., Holst J. C., Olsen M. B. and Bizzarro M. (2014) Precise measurement of chromium isotopes by MC-ICPMS. *J. Anal. At. Spectrom.* **29**, 1406–1416.

Schönberg R., Merdian A., Holmden C., Kleinhanns I., Haßler K., Wille M. and Reitter E. (2016) The stable Cr isotopic compositions of chondrites and silicate planetary reservoirs. *Geochim. Cosmochim. Acta* **183**, 14–30.

Schönberg R., Zink S., Staubwasser M. and von Blanckenburg F. (2008) The stable Cr isotope inventory of solid Earth reservoirs determined by double spike MC-ICP-MS. *Chem. Geol.* **249**, 294–306.

Scott E., Taylor J. and Keil K. (1993) Origin of ureilite meteorites and implications for planetary accretion. *Geophys. Res. Letts.* **20**, 415–418.

Shukolyukov A. and Lugmair G. W. (2006) Manganese-chromium isotope systematics of carbonaceous chondrites. *Earth Planet. Sci. Lett.* **250**, 200–213.

Singletary S. J. and Grove T. L. (2003) Early petrologic processes on the ureilite parent body. *Meteor. Planet. Sci.* **38**, 95–108.

Stagno V. and Frost D. J. (2010) Carbon speciation in the asthenosphere: experimental measurements of the redox conditions at which carbonate-bearing melts coexist with graphite or diamond in peridotite assemblages. *Earth Planet. Sci. Lett.* **300**, 72–84.

Stagno V., Tange Y., Miyajima N., McCammon C. A., Irifune T. and Frost D. J. (2011) The stability of magnesite in the transition zone and the lower mantle as function of oxygen fugacity. *Geophys. Res. Lett.* **38**, L19309.

Takeda H. (1987) Mineralogy of antarctic ureilites and a working hypothesis for their origin and evolution. *Earth Planet. Sci. Lett.* **81**, 358–370.

Teng F.-Z., Li W.-Y., Ke S., Marty B., Dauphas N., Huang S., Wu F.-Y. and Pourmand A. (2010) Magnesium isotopic composition of the Earth and chondrites. *Geochim. Cosmochim. Acta* **74**, 4150–4166.

Teng F.-Z., Wadhwa M. and Helz R. T. (2007) Investigation of magnesium isotope fractionation during basalt differentiation: Implications for a chondritic composition of the terrestrial mantle. *Earth Planet. Sci. Lett.* **261**, 84–92.

Trinquier A., Birck J.-L. and Allègre C. (2008a) High-precision analysis of chromium isotopes in terrestrial and meteorite samples by thermal ionization mass spectrometry. *J. Anal. At. Spectrom.* **23**, 1565–1574.

Trinquier A., Birck J.-L., Allègre C., Göpel C. and Ulfbeck D. (2008b) ^{53}Mn-^{53}Cr systematics of the early Solar System revisited. *Geochim. Cosmochim. Acta* **72**, 5146–5163.

Trinquier A., Birck J.-L. and Allégre C. J. (2007) Widespread ^{54}Cr heterogeneity in the inner Solar System. *Astrophys. J.* **655**, 1179.

Trinquier A., Elliott T., Ulfbeck D., Coath C., Krot A. N. and Bizzarro M. (2009) Origin of nucleosynthetic isotope heterogeneity in the solar protoplanetary disk. *Science* **324**, 374–376.

Van Kooten E. M. M. E., Wielandt D., Schiller M., Nagashima K., Thomen A., Larsen K. K., Olsen M. B., Nordlund k., Krot A. N. and Bizzarro M. (2016) Isotopic evidence for primordial molecular cloud material in metal-rich carbonaceous chondrites. *Proc. Nat. Acad. Sci.* **113**, 2011–2016.

Walker D. and Grove T. (1993) Ureilite smelting. *Meteoritics* **28**, 629–636.

Warren P. H. (2011) Stable isotopes and the noncarbonaceous derivation of ureilites, in common with nearly all differentiated planetary materials. *Geochim. Cosmochim. Acta* **75**, 6912–6926.

Warren P. H. (2012) Parent body depth-pressure-temperature relationships and the style of the ureilite anatexis. *Meteor. Planet. Sci.* **47**, 209–227.

Warren P. H. and Huber H. (2006) Ureilite petrogenesis: a limited role for smelting during anatexis and catastrophic disruption. *Meteor. Planet. Sci.* **41**, 835–849.

Warren P. H. and Kallemeyn G. W. (1988) A new model for ureilite origin: incomplete impact-disruption of partially molten asteroids. *Lun. Planet. Sci. Conf.* **19**, 1238–1239.

Warren P. H. and Kallemeyn G. W. (1992) Explosive volcanism and the graphite-oxygen fugacity buffer on the parent asteroid (s) of the ureilite meteorites. *Icarus* **100**, 110–126.

Warren P. H. and Rubin A. E. (2010) Pyroxene-selective impact smelting in ureilites. *Geochim. Cosmochim. Acta* **74**, 5109–5133.

Wilding M., Benmore C., Tangeman J. and Sampath S. (2004) Evidence of different structures in magnesium silicate liquids: coordination changes in forsterite- to enstatite-composition glasses. *Chem. Geol.* **213**, 281–291.

Woolley A. and Kjarsgaard B. (2008) Paragenetic types of carbonatite as indicated by the diversity and relative abundances of associated silicate rocks: evidence from a global database. *Can. Min.* **46**, 741–752.

Xiao Y., Teng F.-Z., Zhang H.-F. and Yang W. (2013) Large magnesium isotope fractionation in peridotite xenoliths from eastern North China craton: product of melt-rock interaction. *Geochim. Cosmochim. Acta* **115**, 241–261.

Yamakawa A., Yamashita K., Makishima A. and Nakamura E. (2010) Chromium isotope systematics of achondrites: chronology and isotopic heterogeneity of the inner solar system bodies. *Astrophys. J.* **720**, 150.

Yang W., Teng F.-Z., Zhang H.-F. and Li S.-G. (2012) Magnesium isotopic systematics of continental basalts from the North China craton: implications for tracing subducted carbonate in the mantle. *Chem. Geol.* **328**, 185–194.

Zhang G.-L., Chen L.-H., Jackson M. and Hofmann A. (2017) Evolution of carbonated melt to alkali basalt in the South China Sea. *Nat. Geosci.* **10**, 229–235.

Zolensky M., Herrin J., Mikouchi T., Ohsumi K., Friedrich J., Steele A., Rumble D., Fries M., Sandford S., Milam S., Hagiya K., Takeda H., Satake W., Kurihara T., Colbert M., Hanna R., Maisan J., Ketcham R., Goodrich C., Le L., Robinson G., Martinez J., Ross K., Jenniskens P. and Shaddad M. (2010) Mineralogy and petrography of the Almahata Sitta ureilite. *Meteor. Planet. Sci.* **45**, 1618–1637.

Associate Editor: James M.D. Day